NASA Contractor Report 4212

Numerical Simulation and Comparison of Symmetrical/Supercritical Airfoils for the Near Tip Region of a Helicopter in Forward Flight

F. F. Badavi
Planning Research Corporation
Aerospace Technologies Division
Hampton, Virginia

Prepared for
Langley Research Center
under Contract NAS1-18000

National Aeronautics
and Space Administration

Scientific and Technical
Information Division

1989

ABSTRACT

A Navier-Stokes (N-S) equations solver named HEFTA (HElicopter Flow Transonic Analysis) is developed to demonstrate the advantage of computational fluid dynamics (CFD) for the prediction of airloads and acoustics properties. HEFTA's primary emphasis is on a onebladed helicopter rotor in hover or forward flight at transonic tip condition. The solver is based on a three dimensional, time accurate, compressible, thin-layer Reynolds-averaged formulation. The equations are solved in an inertial coordinate system on a body-conformed curvilinear grid of C-H topology. The major emphasis of the initial phase of this work is the study of the aerodynamics of the shock wave boundary layer interaction. Detailed boundary layer and global numerical comparisons of NACA-0012 symmetrical and CAST7-158 supercritical airfoils are made under identical hover and forward flight conditions. The rotor wake effects are modeled by applying a correction to the geometrical angle of attack of the rotor blade. This correction is obtained by computing the local induced downwash velocity as computed by CAMRAD. The coupling of HEFTA and CAMRAD is accomplished in order to place the airfoil in its proper wake environment. The calculations are performed on the Numerical Aerodynamics Simulation (NAS) Cray 2 and on the VPS 32 (a derivative of Cyber 205 at Langley Research Center) for a model helicopter in hover and forward flight.

SYMBOLS

a_∞	speed of sound
c_d, c_{d_p}, c_{d_f}	total, pressure and skin friction drag coefficients
c_f -	skin friction coefficient, $c_f = \tau_w \Big/ \frac{1}{2} \rho_e u_e^2$
c_p	pressure coefficient, $c_p = (p - p_\infty) \Big/ \frac{1}{2} \rho_\infty u_\infty^2$
c	characteristic length scale (chord of the rotor blade, taken as unity)
C	constant in Sutherland's equation
e	total energy per unit volume, nondimensionalized by $\vec{\rho}_\infty \vec{a}_\infty^2$
F, F_v; G, G_v; H, H_v	inviscid and viscous flux vectors of mass, momentum, and energy
I	identity matrix
H	boundary layer shape factor, $H = \delta^*/\theta^*$
J	Jacobian of coordinate transformation
M_∞, M_t	free stream and blade tip Mach number
Δn, Δs	mesh spacings normal and tangential to the airfoil in physical space
Pr	Prandtl number
p, p_∞	local and free stream static pressures (p nondimensionalized by $\vec{\rho}_\infty \vec{a}_\infty^2$)
Q	conservative variable vector
R	radius of rotor blade
R_{e_t}	tip Reynolds number $R_e = \rho_\infty u_t c/\mu_\infty$
r	radial distance from center of rotation
S	viscous stress vector
t	time (nondimensionalized by $R/\vec{a}_\infty$)
T	temperature, also transpose of a matrix quantity
u_∞, u_e	free stream and edge of viscous layer velocities
u, v, w	components of velocity in physical space (nondimensionalized by $\vec{a}_\infty$)
U, V, W	contravariant components of velocity in computational space

$\overline{X}, \overline{X}_b$	inertial and blade fixed coordinates
x, y, z	coordinates in physical space
γ	specific heat ratio
α_i, α_e	induced and effective angles of attack
ξ, η, ζ	transformed coordinates in computational space
κ	thermal conductivity
λ	coefficient of bulk viscosity
μ	viscosity, also advance ratio $\mu = u_\infty/\Omega R$
μ_e, μ_t	effective and turbulent eddy viscosities
ξ_x, ξ_y, ξ_z	metrics of transformation
$\rho, \rho_e, \rho_\infty$	local, edge and free stream fluid densities
ψ	azimuth angle
Ω	angular velocity of rotor blade
δ^*	boundary layer displacement thickness, $\delta^* = \int_0^\delta \left(1 - \frac{\rho u}{\rho_e u_e}\right) dz$
θ^*	boundary layer momentum thickness, $\theta^* = \int_0^\delta \frac{\rho u}{\rho_e u_e}\left(1 - \frac{u}{u_e}\right) dz$
θ_c	geometric angle of attack
τ_w	wall shear stress, $\tau_w = \mu \left(\frac{\partial u}{\partial z}\right)_{z=0}$
τ	time in computational space
$\tau_{xx}, \tau_{xy}, \tau_{yy}, \ldots$	viscous derivative terms
ν	kinematic viscosity

Subscripts and Superscripts

∞, e, w	conditions at infinity, edge of viscous layer and wall
$\xi, \eta, \zeta; x, y, z$	derivatives with respect to $\xi, \eta, \zeta; x, y, z$
$\wedge$	quantities in computational space
$\sim$	quantities in rotating coordinate frame
$\rightarrow$	denotes dimensional quantities

I. INTRODUCTION

The flow around rotor blades is a complex phenomenon involving transonic flow with associated shock wave boundary layer interaction. This results in shock induced flow separation, blade vortex interaction on the advancing blade, and dynamic stall on the retreating blade. Other aerodynamic complexities, such as rotor fuselage interactions, aeroacoustic effects, and the overall unsteady nature of the rotorcraft flow field caused by aeroelastic effects, impose major limitations on the high speed transonic flight of rotorcraft. These limitations are manifested through undesirably high vibration levels, power divergence, noise, and component fatigue. These different phenomena can not be computed accurately by one single method. For this reason, highly specialized methods are required for any particular aspect of rotor blade aerodynamics. For many years, helicopter designers have used a mixture of simplified integral methods, such as panel and lifting surface computer codes, wind tunnel data, and design charts, to perform numerical analyses with the knowledge that the technique of combining traditional integral methods, with experimental data for computing rotorcraft aerodynamics loads is unable to compute the full impact of transonic effects.

Numerous investigators have addressed the limitations of integral methods by using nonlinear finite difference methods to compute the aerodynamics of rotor blades. Finite difference methods provide the technique to compute the entire nonlinear flow field about the rotor blade at transonic speeds. The primary difference between linear integral methods and nonlinear finite difference methods is that linear solutions depend only on shear layer conditions and blade surface while finite difference solutions depend on the entire flow field. The finite difference methods also have the advantage of being designed to compute the transonic flow nonlinearities associated with high speed advancing blades. They have progressed from the solution of transonic small disturbance equations to full potential equations and more recently to the Euler and Navier-Stokes (N-S) equations.

In this work, an N-S solver for calculating the viscous transonic flow on rotor blades in hover and forward flight is described. The time accurate, unsteady, thin layer N-S equations are solved in an inertial frame of reference, rather than in a blade fixed rotating reference. This provides a unified scheme which has the capacity of handling both hover and forward flight in an identical manner. This approach results in an increase of CPU time, but allows the same overall formulation to be used for both hover and forward flight.

For the calculation of viscous transonic flow about hovering or advancing rotor blades, the N-S equations describe shock location, pressure and skin friction drag and vortical motion accurately. Calculation of vortical motion for the rotor blade flow field is significant since the field is characterized by blade vortex interaction (BVI) and ,in particular, by complex vortical wakes. These must be accounted for in order to describe the forces acting on hovering or advancing rotor blades. Figure 1 shows the profile of the vortical sheets in hover mode as they pass through the rotor blade. For vortical wakes, the contraction of the helical wake as it passes through and below into the rotor disk and the interaction of the tip vortex of one rotor blade with the following are significant. The vortex distention and contraction depends on the downwash velocity which significantly influences the accuracy of loads prediction on the blade.

In this work, the rotor wake effects in forward flight are modeled in the form of a correction to the geometric angle of attack of the rotor blade.This correction, depending on the flow conditions, varies along the blade span and azimuth direction, and reduces the geometric angle of attack θ_c. So far, most hover and forward flight calculations have depended on this vortex induced surface inflow boundary condition method which has proven to be farily successful for moderate to high advance ratios where total flow is much larger than induced flow. The modeling of wake effects is done by the use of the free wake analysis program CAMRAD (ref. 1). This choice of calculation procedure is due to the fact that lifting rotors in forward flight have wake systems that are too complex to be modeled in the current N-S equations solvers. In addition, there is not a straightforward way to couple the blade trim solution directly into any finite difference scheme. With this approach and others (ref. 2), estimates of the downwash velocity v_i and corresponding induced angle of attack α_i are obtained from free wake analysis calculations. Since α_i has a negative value, the influence of the vortical wake is to reduce the geometric angle of attack so that an effective angle of attack $\alpha_e = \theta_c - \alpha_i$ is obtained.

In CAMRAD aerodynamic loads are calculated by computing induced angles of attack along the rotor span which are the result of the trimmed rotor and wake system. The blade lift coefficients are then decided through table lookups of two dimensional airfoil data. The coupling between HEFTA and

CAMRAD for a set of specified induced angles of attack is accomplished by replacing the table lookups with lift coefficients that are calculated from HEFTA. This process starts by calculating a trimmed solution from CAMRAD where the spanwise lift coefficients are completely obtained from airfoil tables. CAMRAD then determines a spanwise set of wake induced angles along the rotor surface. The calculated inflow angles are then used to model the wake effects in HEFTA. HEFTA then produces a set of unsteady lift coefficients which are applied to the subsequent CAMRAD trim solution stage. This iterative process continues until the values of induced angles of attack does not change.

In this work, a previously developed ,three-dimensional, fixed wing, thin layer N-S equations solver (refs. 3) is modified to simulate the transonic flow field about rotor blade. An inertial coordinate system is used on a body conformed curvilinear grids around the blade. A modular solution approach is adopted where an independently generated, body fitted grid of C-H topology (C, in wraparound radial direction and H, in the spanwise direction) is coupled with the N-S equations solver. The three dimensional C-H grid was generated by assembling two dimensional spanwise sectional C-grids. The two dimensional C-grid around the blade is generated by the application of an in-house algebraic grid generation procedure. The N-S equations solver is developed with an implicit, upwind-biased, finite volume scheme which uses the Van Leer's flux vector splitting and the Beam-Warming's approximate factorization of the conservative form of the Reynolds-averaged, thin layer N-S equations to obtain the flowfield quantities. Modifications were necessary to implement the rotation matrix into the flow solver to accurately solve the rotor blade flow field.

Part II describes the governing equations and numerical scheme. Part III presents the computational results. Part IV describes the near future plans for the present algorithm and the conclusions.

II. GOVERNING EQUATIONS AND NUMERICAL SCHEME

Problem Formulation

The time dependent compressible N-S equations express the conservation of mass, momentum, and energy for an ideal gas in the absence of external forces. The strong conservative law form of the N-S equations are used for shock capturing purposes. The equations in Cartesian coordinates in nondimensional form can be written as

$$\frac{\partial Q}{\partial t}+\frac{\partial F}{\partial x}+\frac{\partial G}{\partial y}+\frac{\partial H}{\partial z}=\frac{\partial F_v}{\partial x}+\frac{\partial G_v}{\partial y}+\frac{\partial H_v}{\partial z} \tag{1}$$

where

$$\begin{aligned}
Q &= \{\rho, \rho u, \rho v, \rho w, e\}^T \\
F &= \left\{\rho u, \rho u^2+p, \rho uv, \rho uw, u(e+p)\right\}^T \\
G &= \left\{\rho v, \rho uv, \rho v^2+p, \rho vw, v(e+p)\right\}^T \\
H &= \left\{\rho w, \rho uw, pvw, \rho w^2+p, w(e+p)\right\}^T \\
F_v &= Re^{-1}\left\{0, \tau_{xx}, \tau_{yx}, \tau_{zx}, \beta_x\right\}^T \\
G_v &= Re^{-1}\left\{0, \tau_{xy}, \tau_{yy}, \tau_{zy}, \beta_y\right\}^T \\
H_v &= Re^{-1}\left\{0, \tau_{xz}, \tau_{yz}, \tau_{zz}, \beta_z\right\}^T
\end{aligned} \tag{2}$$

with

$$\begin{gathered}
\tau_{xx} = \lambda\left(u_x + v_y + w_z\right) + 2\mu u_x \\
\tau_{yy} = \lambda\left(u_x + v_y + w_z\right) + 2\mu v_y \\
\tau_{zz} = \lambda\left(u_x + v_y + w_z\right) + 2\mu w_z \\
\tau_{xy} = \tau_{yx} = \mu\left(u_y + v_x\right) \\
\tau_{xz} = \tau_{zx} = \mu\left(u_z + w_x\right) \\
\tau_{yz} = \tau_{zy} = \mu\left(v_z + w_y\right) \\
\beta_x = \gamma\ \kappa Pr^{-1} \partial_x e_I + u\tau_{xx} + v\tau_{xy} + w\tau_{xz} \\
\beta_y = \gamma\ \kappa Pr^{-1} \partial_y e_I + u\tau_{yx} + v\tau_{yy} + w\tau_{yz} \\
\beta_z = \gamma\ \kappa Pr^{-1} \partial_z e_I + u\tau_{zx} + v\tau_{zy} + w\tau_{zz} \\
e_I = e\rho^{-1} - 0.5\left(u^2 + v^2 + w^2\right)
\end{gathered} \tag{3}$$

The Cartesian velocity components u, v, and w are nondimensionalized by the free stream speed of sound a_∞.

A general three dimensional curvilinear transformation between the Cartesian variables (x,y,z) and the generalized coordinates (ξ,η,ζ) is applied to (1), where ζ corresponds to the coordinate normal to the body surface. The vector Q represents density, momentum, and total energy per unit volume, and p is the pressure defined from the equation of state of an ideal gas as

$$p = (\gamma - 1)\left[e - \frac{\rho}{2}\left(u^2 + v^2 + w^2\right)\right] \tag{4}$$

The transformation from (x,y,z) to (ξ,η,ζ) is defined as

$$\begin{gathered}
\tau = t \\
\xi = \xi(x,y,z,t) \\
\eta = \eta(x,y,z,t) \\
\zeta = \zeta(x,y,z,t)
\end{gathered} \tag{5}$$

The resulting transformed equations in nondimensional form are written as

$$\frac{\partial}{\partial\tau}\hat{Q}+\frac{\partial}{\partial\xi}\left(\hat{F}-\hat{F}_v\right)+\frac{\partial}{\partial\eta}\left(\hat{G}-\hat{G}_v\right)+\frac{\partial}{\partial\zeta}\left(\hat{H}-\hat{H}_v\right)=0 \qquad (6)$$

where

$$\begin{aligned}
\hat{Q} &= J^{-1}\{\rho, \rho u, \rho v, \rho w, e\}^T\\
\hat{F} &= J^{-1}\left\{\rho U, \rho uU+\xi_x p, \rho vU+\xi_y p, \rho wU+\xi_z p, (e+p)U-\xi_t p\right\}^T\\
\hat{G} &= J^{-1}\left\{\rho V, \rho uV+\eta_x p, \rho vV+\eta_y p, \rho wV+\eta_z p, (e+p)V-\eta_t p\right\}^T\\
\hat{H} &= J^{-1}\left\{\rho W, \rho uW+\zeta_x p, \rho vW+\zeta_y p, \rho wW+\zeta_z p, (e+p)W-\zeta_t p\right\}^T
\end{aligned} \qquad (7)$$

and

$$\begin{aligned}
U &= \xi_t+\xi_x u+\xi_y v+\xi_z w\\
V &= \eta_t+\eta_x u+\eta_y v+\eta_z w\\
W &= \zeta_t+\zeta_x u+\zeta_y v+\zeta_z w
\end{aligned} \qquad (8)$$

where U, V, and W are contravariant velocity components written without metric normalization. The corresponding viscous flux terms are

$$\begin{aligned}
\hat{F}_v &= J^{-1}Re^{-1}\left\{0, \xi_x\tau_{xx}+\xi_y\tau_{xy}+\xi_z\tau_{xz}, \xi_x\tau_{yx}+\xi_y\tau_{yy}+\xi_z\tau_{yz}, \xi_x\tau_{zx}+\xi_y\tau_{zy}+\xi_z\tau_{zz}, \xi_x\beta_x+\xi_y\beta_y+\xi_z\beta_z\right\}^T\\
\hat{G}_v &= J^{-1}Re^{-1}\left\{0, \eta_x\tau_{xx}+\eta_y\tau_{xy}+\eta_z\tau_{xz}, \eta_x\tau_{yx}+\eta_y\tau_{yy}+\eta_z\tau_{yz}, \eta_x\tau_{zx}+\eta_y\tau_{zy}+\eta_z\tau_{zz}, \eta_x\beta_x+\eta_y\beta_y+\eta_z\beta_z\right\}^T\\
\hat{H}_v &= J^{-1}Re^{-1}\left\{0, \zeta_x\tau_{xx}+\zeta_y\tau_{xy}+\zeta_z\tau_{xz}, \zeta_x\tau_{yx}+\zeta_y\tau_{yy}+\zeta_z\tau_{yz}, \zeta_x\tau_{zx}+\zeta_y\tau_{zy}+\zeta_z\tau_{zz}, \zeta_x\beta_x+\zeta_y\beta_y+\zeta_z\beta_z\right\}^T
\end{aligned}$$

(9)

where the components of heat flux vectors and shear stress tensors in nondimensional form were given in (3).

Applying chain rule relations, the Cartesian derivatives in generalized coordinates (ξ,η,ζ) become

$$\begin{aligned}
u_x &= \xi_x u_\xi + \eta_x u_\eta + \zeta_x u_\zeta \\
u_y &= \xi_y u_\xi + \eta_y u_\eta + \zeta_y u_\zeta \\
u_z &= \xi_z u_\xi + \eta_z u_\eta + \zeta_z u_\zeta
\end{aligned} \tag{10}$$

and the transformation metrics become

$$\begin{aligned}
\xi_x &= J\left(y_\eta z_\zeta - y_\zeta z_\eta\right) \\
\xi_y &= J\left(z_\eta x_\zeta - x_\eta z_\zeta\right) \\
\xi_z &= J\left(x_\eta y_\zeta - y_\eta x_\zeta\right) \\
\zeta_x &= J\left(y_\xi z_\eta - z_\xi y_\eta\right) \\
\zeta_y &= J\left(x_\eta z_\xi - x_\xi z_\eta\right) \\
\zeta_z &= J\left(x_\xi y_\eta - y_\xi x_\eta\right) \\
\eta_x &= J\left(z_\xi y_\zeta - y_\xi z_\zeta\right) \\
\eta_y &= J\left(x_\xi z_\zeta - x_\zeta z_\xi\right) \\
\eta_z &= J\left(y_\xi x_\zeta - x_\xi y_\zeta\right) \\
\xi_t &= -x_\tau \xi_x - y_\tau \xi_y - z_\tau \xi_z \\
\eta_t &= -x_\tau \eta_x - y_\tau \eta_y - z_\tau \eta_z \\
\zeta_t &= -x_\tau \zeta_x - y_\tau \zeta_y - z_\tau \zeta_z
\end{aligned} \tag{11}$$

where J is the Jacobian of the transformation and is given by

$$J = \xi_x\left(\eta_x \zeta_z - \eta_z \zeta_y\right) + \xi_y\left(\eta_z \zeta_x - \eta_x \zeta_z\right) + \xi_z\left(\eta_x \zeta_y - \eta_y \zeta_x\right) \tag{12}$$

Since the dominant viscous effects of high Reynolds number turbulent flow arises from viscous diffusion normal to the body surface, a thin layer assumption is employed. Only the viscous diffusion terms normal to the body surface are retained and all viscous derivatives along the body in ξ, η direction are dropped. That leads to thin layer N-S equations as

$$\frac{\partial \hat{Q}}{\partial \tau}+\frac{\partial \hat{F}}{\partial \xi}+\frac{\partial \hat{G}}{\partial \eta}+\frac{\partial \hat{H}}{\partial \zeta}=\mathrm{Re}^{-1}\frac{\partial \hat{S}}{\partial \zeta} \tag{13}$$

where

$$\begin{aligned}\hat{S}=J^{-1}\Big\{&0,\ \mu\left(\zeta_x^2+\zeta_y^2+\zeta_z^2\right)\mu_\zeta+(\mu/3)\left(\zeta_x u_\zeta+\zeta_y v_\zeta+\zeta_z w_\zeta\right)\zeta_x,\ \mu\left(\zeta_x^2+\zeta_y^2+\zeta_z^2\right)v_\zeta\\ &+(m/3)\left(\zeta_x u_\zeta+\zeta_y v_\zeta+\zeta_z w_\zeta\right)\zeta_y,\ \mu\left(\zeta_x^2+\zeta_y^2+\zeta_z^2\right)w_\zeta+(\mu/3)\left(\zeta_x u_\zeta+\zeta_y v_\zeta+\zeta_z w_\zeta\right),\ \Big\{\left(\zeta_x^2+\zeta_y^2+\zeta_z^2\right)\\ &\times\left[0.5\mu\left(u^2+v^2+w^2\right)_\zeta+\mu \mathrm{Pr}^{-1}(\gamma-1)^{-1}\left(a_\infty^2\right)_\zeta\right]+(\mu/3)\left(\zeta_x u+\zeta_y v+\zeta_z w\right)\times\left(\zeta_x u_\zeta+\zeta_y v_\zeta+\zeta_z w_\zeta\right)\Big\}\Big\}^T\end{aligned} \tag{14}$$

In the above equations, u, v, w are the velocity components in the inertial rotor reference frame (x,y,z,t) and (13) is solved in this frame. The inertial coordinate $\overline{X}=(x,y,z,t)$ is related to the blade fixed coordinate $\overline{X}_b=(\tilde{x},\tilde{y},\tilde{z},\tilde{t})$ by

$$\begin{aligned}&\overline{X}(x,y,z)=R(t)\overline{X}_b(\tilde{x},\tilde{y},\tilde{z})\\ &t=\tilde{t}\end{aligned} \tag{15}$$

where R(t) is the rotation matrix (ref. 4) and is given by

$$R(t)=\begin{bmatrix}\cos\Omega\tilde{t} & -\sin\Omega\tilde{t} & 0\\ \sin\Omega\tilde{t} & \cos\Omega\tilde{t} & 0\\ 0 & 0 & 1\end{bmatrix} \tag{16}$$

and Ωt represents the azimuthal sweep of the rotor blade. This establishes a relation between metric quantities in the inertial and blade fixed frames as (ref. 5)

$$
\begin{aligned}
&\xi_x = \xi_{\tilde{x}} \cos \Omega \tilde{t} - \xi_{\tilde{y}} \sin \Omega \tilde{t} \\
&\xi_y = \xi_{\tilde{x}} \sin \Omega \tilde{t} + \xi_{\tilde{y}} \cos \Omega \tilde{t} \\
&\xi_z = \xi_{\tilde{z}} \\
&\eta_x = \eta_{\tilde{x}} \cos \Omega \tilde{t} - \eta_{\tilde{y}} \sin \Omega \tilde{t} \\
&\eta_y = \eta_{\tilde{x}} \sin \Omega \tilde{t} + \eta_{\tilde{y}} \cos \Omega \tilde{t} \\
&\eta_z = \eta_{\tilde{z}} \\
&\zeta_x = \zeta_{\tilde{x}} \cos \Omega \tilde{t} - \zeta_{\tilde{y}} \sin \Omega \tilde{t} \\
&\zeta_y = \zeta_{\tilde{x}} \sin \Omega \tilde{t} + \zeta_{\tilde{y}} \cos \Omega \tilde{t} \\
&\zeta_z = \zeta_{\tilde{z}} \\
&\xi_t = \Omega \tilde{y} \xi_{\tilde{x}} - \Omega \tilde{x} \xi_{\tilde{y}} \\
&\eta_t = \Omega \tilde{y} \eta_{\tilde{x}} - \Omega \tilde{x} \eta_{\tilde{y}} \\
&\zeta_t = \Omega \tilde{y} \zeta_{\tilde{x}} - \Omega \tilde{x} \zeta_{\tilde{y}}
\end{aligned}
\tag{17}
$$

Equation (13) is closed by Stokes' hypothesis for bulk viscosity as

$$\lambda + \frac{2}{3}\mu = 0 \tag{18}$$

and Sutherland's law for molecular viscosity as

$$\mu = \left(\frac{T}{T_\infty}\right)^{3/2} \frac{T_\infty + C}{T + C} \tag{19}$$

where T_∞ is freestream temperature ($T_\infty = 460$ R) and C is the Sutherland's constant. All calculations are done under the assumption that the flow over the entire upper surface of the rotor blade is turbulent, which is equivalent to the experimental placement of a transition strip at the leading edge of the blade.

Spatial Differencing

The generalized fluxes $\hat{F}$, $\hat{G}$ and $\hat{H}$, representing pressure and convective terms, are spatially differenced by a second order accurate upwind biased flux vector splitting method, i.e., split into differenced forward and backward contributions and differenced accordingly. For instance, in one dimension the flux difference in the ξ direction is (ref. 6)

$$\delta_\xi \hat{F} = \delta_\xi^- \hat{F}^+ + \delta_\xi^+ \hat{F}^- \tag{20}$$

where δ_ξ^- and δ_ξ^+ denote general backward and forward divided difference operators. The flux vector in three dimensional generalized coordinates is split according to the formulation of Van Leer (refs. 7-8). The flux $\hat{F}$, for example, is split according to the contravariant Mach number in the ξ direction as

$$M_\xi = \frac{\bar{u}}{a_\infty}$$

with (21)

$$\bar{u} = \frac{U}{\nabla \xi}$$

where ∇ represents the gradient operation. For supersonic flow, where $|M_\xi| \geq 1$, $\hat{F}^\pm$ is

$$\left.\begin{aligned} &\hat{F}^{+} = \hat{F} \\ &\hat{F}^{-} = 0 \end{aligned}\right\} \rightarrow M_{\xi} \geq +1 \qquad \left.\begin{aligned} &\hat{F}^{-} = \hat{F} \\ &\hat{F}^{+} = 0 \end{aligned}\right\} \rightarrow M_{\xi} \leq -1 \tag{22}$$

and for subsonic flow where $|M_{\xi}| < 1$, $\hat{F}^{\pm}$ is

$$\hat{F}^{\pm} = \frac{\nabla\xi}{J} \left\{ f^{\pm}_{\text{mass}},\ f^{\pm}_{\text{mass}}\left[\hat{k}_x(-\bar{u} \pm 2a_{\infty})/\gamma + u\right],\ f^{\pm}_{\text{mass}}\left[\hat{k}_y(-\bar{u} \pm 2a_{\infty})/\gamma + v\right], \right.$$
$$\left. f^{\pm}_{\text{mass}}\left[\hat{k}_z(-\bar{u} \pm 2a_{\infty})/\gamma + w\right],\ f^{\pm}_{\text{energy}} \right\}^{T} \tag{23}$$

with

$$f^{\pm}_{\text{mass}} = \pm\rho a_{\infty}(M_{\xi} \pm 1)^2/4$$
$$f^{\pm}_{\text{energy}} = f^{\pm}_{\text{mass}}\left[\left\{-(\gamma-1)\bar{u}^2 \pm 2(\gamma-1)\bar{u}a_{\infty} + 2a_{\infty}^2\right\}/\left(\gamma^2 - 1\right) + \frac{1}{2}\left(u^2 + v^2 + w^2\right)\right] \tag{24}$$

The equations above are solved with a finite volume approach. In the ξ direction the surface area of the cell surface is $\frac{\nabla\xi}{J}$, the cell volume is J^{-1}, and $(\hat{k}_x, \hat{k}_y, \hat{k}_z)$ are the direction cosines of the cell interface in the ξ direction and are defined as

$$\left(\hat{k}_x, \hat{k}_y, \hat{k}_z\right) = \frac{(\xi_x, \xi_y, \xi_z)}{\nabla\xi} \tag{25}$$

For $\Delta\xi = \Delta\eta = \Delta\zeta = 1$, the implementation of split flux differences are done by a flux balance across the i-th cell holding spatial indices j and k constant as

$$\delta_\xi^- \hat{F}_i^+ + \delta_\xi^+ \hat{F}_i^- = \left[\hat{F}^+\left(Q^-\right) + \hat{F}^-\left(Q^+\right)\right]_{i+1/2} - \left[\hat{F}^+\left(Q^-\right) + \hat{F}^-\left(Q^+\right)\right]_{i-1/2} \tag{26}$$

where $\hat{F}^+\left(Q^-\right)_{i+1/2}$ refers to a forward flux evaluated using the metric terms at the cell interface i + 1/2, and the state variable, Q, is obtained by the upwind second order interpolation of cell centered variables as

$$\begin{aligned} Q^-_{i+1/2} &= 3/2\,Q_i - 1/2\,Q_{i-1} \\ Q^+_{i+1/2} &= 3/2\,Q_{i+1} - 1/2\,Q_{i+2} \end{aligned} \tag{27}$$

For the diffusion terms representing shear stress and heat transfer effects, the fluxes are differenced through a second order central difference scheme where second derivatives are treated as differences across cell interfaces of first derivative terms, holding spatial indices i and j constant, as

$$\delta_\zeta \hat{H}_{v_k} = \hat{H}_{v_{k+1/2}} - \hat{H}_{v_{k-1/2}} \tag{28}$$

where

$$\hat{H}_v = \frac{M_\infty \mu}{Re_\ell J}\left\{0,\ \phi_1 u_\zeta + \zeta_x \phi_2,\ \phi_1 v_\zeta + \zeta_y \phi_2,\ \phi_1 w_\zeta + \zeta_z \phi_2,\ \phi_1\left[\left(\frac{q^2}{2}\right)_\xi + (\gamma - 1)^{-1} Pr^{-1}\left(a_\infty^2\right)_\zeta\right] + W\phi_2\right\}^T \tag{29}$$

where q is the heat flux term and

$$\begin{aligned}&\phi_1 = \zeta_x^2 + \zeta_y^2 + \zeta_z^2\\&\phi_2 = \left(\zeta_x u_\zeta + \zeta_y v_\zeta + \zeta_z w_\zeta\right)/3\\&\delta_\zeta u_{k+1/2} = u_{k+1} - u_k\end{aligned}\tag{30}$$

Time Differencing

The linearized, backward time approximation in delta form for three dimensional equations is given by

$$\left[\frac{I}{J\Delta t} + \delta_\xi \frac{\partial \widehat{F}}{\partial Q} + \delta_\eta \frac{\partial \widehat{G}}{\partial Q} + \delta_\zeta\left(\frac{\partial \widehat{H}}{\partial Q} - \frac{\partial \widehat{H}_v}{\partial Q}\right)\right]\Delta Q = -L\left(Q^n\right)\tag{31}$$

with $L(Q^n)$ as the discrete representation of the spatial derivative terms in (13) evaluated at time step n. The above equation (31) is spatially factored (ref. 9) and solved as a series of sweeps through the mesh as

$$\begin{aligned}&\left[\frac{I}{J\Delta t} + \delta_n \frac{\partial \widehat{G}}{\partial Q}\right]\Delta Q^{\bullet} = -L\left(Q^n\right)\\&\left[\frac{I}{J\Delta t} + \delta_\zeta\left(\frac{\partial \widehat{H}}{\partial Q} - \frac{\partial \widehat{H}_v}{\partial Q}\right)\right]\Delta Q^{**} = \left(\frac{I}{J\Delta t}\right)\Delta Q^{*}\\&\left[\frac{I}{J\Delta t} + \delta_\xi \frac{\partial \widehat{F}}{\partial Q}\right]\Delta Q = \left(\frac{I}{J\Delta t}\right)\Delta Q^{**}\end{aligned}\tag{32}$$

where

$$\Delta Q = Q^{n+1} - Q^n\tag{33}$$

Turbulence Modeling

Due to the high Reynolds number of the flow, it is assumed that the entire upper surface of the rotor blade is turbulent. In the governing equations, the effect of turbulence is accounted for through the concept of eddy viscosity. In the momentum equations, the molecular viscosity μ is replaced by an effective viscosity μ_e as

$$\mu_e = \mu + \mu_t \tag{34}$$

where μ_t is the turbulent viscosity and the Baldwin Lomax (ref. 10) algebraic turbulence model is used to evaluate the turbulent quantities. The turbulent viscosity term, μ_t, plays an important role in shaping the boundary layer and tip vortex formation profiles. In high Reynolds number transonic flow ,the rapid thickening of the boundary layer influences the location and strength of any shock that may be present.

Far Field Boundary Conditions

Depending on the nature of the flow at the boundary (inflow vs. outflow, subsonic vs. supersonic),flow field quantities are either fixed or extrapolated from the interior. A compressible two-dimensional line vortex solution (ref. 11) is used for far field velocities that are fixed. This method is only used for steady problems due to the time lag of the circulation on the blade and its effect on the far field flow. For unsteady cases the far field velocities are set equal to zero when not extrapolated.

Blade Surface Boundary Conditions

At the surface of the blade, the no slip conditions are used with the transpiration velocity modifications to include the effects of the wake. With the transpiration method the velocity at the blade surface is set equal to downwash velocity instead of zero, where downwash velocity is given by

$$v_{wake} = \left(\Omega y + V_\infty \sin\psi \cos\alpha_{TPP}\right) \tan\alpha_e \tag{35}$$

Grid Methodology

A modular solution approach is adopted where an independently generated, body-conformed grid of C-H topology (C in wraparound-radial direction and H in the spanwise direction) of 351 x 80 x 21 cells in the ξ, η, ζ directions is coupled to the flow solver. This block, with over half a million grid cells, was generated by an assembly of 21, two dimensional spanwise sectional C-grids. The two dimensional C-grid around the blade is generated by the application of an in-house algebraic grid generation procedure. Figure 2 presents the section profiles of the supercritical airfoil CAST7-158 and the symmetrical airfoil NACA-0012. The half thickness profiles and camber profiles of each airfoil are also included. Note that the camber profile of the supercritical airfoil is quite different than the straight line profile of the symmetrical airfoil. Figure 3 presents the partial view of the C-grid profile for the two airfoils with 351 wraparound and 80 radial points. In the radial direction the grid lines are heavily stretched to resolve the viscous sublayer. The minimum grid spacing in the radial direction is $2 \times 10^{-5}c$ (c=chord) which corresponds to the value of $y^+ = 3$ at a tip Reynolds number of 5×10^6. In the wraparound direction, the important requirements are that the grid lines are clustered in regions where steep gradients of flow variables are expected (i.e., at the leading edge, trailing edge and near blade tip) and that a smooth and continuous change of the size of the adjacent grid cells is maintained. The C-grid is stretched 5 chords from the rotor surface in the wraparound and normal direction, and spanwise grid distributions have inner boundaries located 4 chords from the rotor tip. The outer spanwise grid boundary is located approximately 2 chords beyond the tip of the rotor blade. The rotor blade itself is untapered and untwisted and is not conically faired at the tip (i.e., sharp edged tip). In the spanwise direction, a nonuniform distribution of C-grid planes is used to concentrate the two dimensional planes near the tip region. A simplified schematic of the entire C-H grid block with the embedded blade rotor is shown in figure 4 with C-grid planes extending outward in the spanwise direction.

The C-grid plane is transformed into a generalized coordinate system as

$$\begin{aligned} \xi &= \xi\,(x, y_C, z, t) \\ \zeta &= \zeta\,(x, y_C, z, t) \qquad (36) \\ \tau &= t \end{aligned}$$

where y_C refers to a constant value of spanwise location. The transformation allows the boundary surfaces in the physical plane to be mapped into rectangular surfaces in the computational plane. This transformation simplifies the boundary condition requirements in the computational domain and allows grid points to be clustered in the physical plane in regions of steep gradients. Figure 5 taken from reference 12 shows this transformation with the section in the trailing edge enlarged to show the high aspect ratio $\Delta s/\Delta n$ requirements in the viscous sublayer.

III. COMPUTATIONAL RESULTS

The primary purpose of this work is to numerically compare the behavior of transonic flow of a 12% thick supercritical airfoil section (CAST7-158) with that of a symmetrical airfoil section (NACA-0012) under identical forward flight conditions to draw conclusions concerning the blade performance and noise propagation in the near tip region of a rotor blade. This is accomplished by performing computations with the following flight conditions:

$M_t = 0.86$
$\theta_C = 8°$
$\psi = 90°$
$\mu = 0.3$
$Re_t = 5 \times 10^6$
$y/R = 0.96, 0.90, 0.80, 0.70$

where M_t is the tip mach number, θ_C is the collective pitch, ψ is the azimuthal angle of rotor disk, μ is the advance ratio, Re_t is the Reynolds number at rotor tip, and y/R is the spanwise locations where computation is performed. The untapered and untwisted rotor blade has an aspect ratio of 6 and has a

CAST7-158 or NACA-0012 airfoil section profile. A typical computation requires 18 x 10^6 words of memory and 2 x 10^{-5} seconds of CPU time per grid point per iteration.

Performance

Figure 6 presents the surface pressure distribution for CAST7-158 (solid line) and NACA-0012 (dashed line) at $\psi = 90°$ and y/R = 0.96, 0.90, 0.80, 0.70. It shows that CAST7-158 has retained its attached turbulent flow profile up to x/c ≈ 0.7 while NACA-0012 has a massively separated turbulent profile with a shock position at x/c ≈ 0.4. This difference in shock position is observed at all four locations and accounts for the performance of each blade. Table 1 presents the results of the section lift and drag coefficients with drag being composed of pressure drag and skin friction drag. Due to a delayed ,shock-induced, separated boundary layer, the lift coefficient of CAST7-158 is higher than the NACA-0012 at all four y/R locations. This accounts for the superior performance of the supercritical airfoil over the conventional airfoil at transonic speed.

Boundary Layer Quantities

Figures 7(a) - 7(h) present the boundary layer velocity profiles for the CAST7-158 (solid line) and the NACA-0012 (dashed line), normalized by the velocity at the edge of the boundary layer, at x/c = 0.01, 0.10, 0.44, 0.57, 0.67, 0.75, 0.86, 0.99 and y/R = 0.96, 0.90, 0.80, 0.70. Only the very narrow viscous sublayer with a maximum height of z/c = 0.004 is shown to study the behavior of two airfoils very near the blade surface. Figures 7(a) - 7(b) show that at x/c = 0.01 and x/c = 0.10 the velocity profiles of the two airfoils are somewhat similar. This is due to the fact that near the leading edge of the rotor blade, the flow is attached and a separation zone does not exist, which was also observed on the c_p plots of Figure 6. Figures 7(c) - 7(d) at x/c = 0.44 and x/c = 0.57 are immediately to the aft of the shock position on the NACA-0012 and show an unfavorable velocity profile for the NACA-0012 compared to the CAST7-158 for all four y/R locations. This unfavorable profile is caused by an adverse pressure gradient behind the shock location which causes the u component of velocity to slow down and eventually generate a very weak circulation near the surface of the blade as is shown by Figure 7(d) at y/R = 0.96 near the tip. The profiles at different y/R stations at these two x/c locations are also of interest. In figure 7(c) the profiles for the two airfoils are somewhat similar near the tip and deviate toward inner locations, while figure 7(d) indicates a small region of flow reversal near the tip and a gradual improvement of the NACA-0012 profile toward the inner locations. These differences are due to the fact that the flow over the NACA-0012 is gradually reattaching itself as it moves toward the aft region of the blade.

A similar situation for the CAST7-158 is shown in figures 7(e) - 7(f) at $x/c = 0.67$ and $x/c = 0.75$ with a shock position at $x/c = 0.7$. Here the region of unfavorable velocity profile near the tip is small and gradually moves toward the inner locations as shown by figure 7(e), which results in a large reversed flow region near the tip at $x/c = 0.75$ and gradual profile improvements toward the inner locations as shown by figure 7(f). Figures 7(g) - 7(h) indicate the possibility of a second smaller reversed flow region for the CAST7-158 near the tip as is shown in figure 7(g) with improvements of the flow profiles in figure 7(h). It must be noted that at the last four x/c locations, namely $x/c = 0.67, 0.75, 0.86, 0.99$, the NACA-0012 has a more favorable profile than the CAST7-158 due to the partial reattachment of the flow at these locations. Therefore, for the first 60% of the upper surface, the CAST7-158 has a more favorable profile, while for the last 40%, the NACA-0012 profiles are more favorable.

Figure 8(a) shows the skin friction coefficient c_f profiles for the upper surface of the CAST7-158 (solid line) and the NACA-0012 (dashed line) at $y/R = 0.96, 0.90, 0.8, 0.70$. The skin friction coefficient is a measure of the frictional forces on the surface of the airfoil. In figure 8(a) a smooth variation of c_f as a function of x/c up to $x/c \approx 0.4$ for the NACA-0012 and $x/c \approx 0.7$ for the CAST7-158 at all four y/R locations is shown. The drop in the value of c_f is the indication of shock-induced boundary layer separation and possible flow reversal as is shown in the figure for all y/R locations. At $y/R = 0.96, 0.90, 0.80$, small negative values of c_f exist which indicate that the boundary layer is not only separated, but also there is a region of reversed flow which gradually weakens as it moves toward the inner region of the blade to reattach itself with the flow.

Figures 8(b) - 8(d) are the displacement thickness δ^*, momentum thickness θ^* (both normalized with respect to chord length), and the shape factor H profiles for the upper surface of the CAST7-158 (solid line) and the NACA-0012 (dashed line) at $y/R = 0.96, 0.90, 0.80, 0.70$. Displacement thickness is a measure of the distance the free stream air flow is displaced outward (i.e., away from the surface) due to the decrease of the velocity in the boundary layer. In analogy to displacement thickness, a momentum thickness can be defined in accordance with momentum principal which can be established by equating the momentum flow loss due to the wall friction in the boundary layer to the momentum flow in the absence of the boundary layer. A value of the shape factor $H \geq 2.5$ is a qualitative measure of flow separation and reversal.

In figures 8(b) - 8(d) a smooth variation of δ^*, θ^*, and H as a function of x/c up to x/c ≈ 0.4 for the NACA-0012 and x/c ≈ 0.7 for the CAST7-158 is shown. An increase in the value of δ^*, θ^* and H is the indication of boundary layer separation and flow reversal and is shown in the figures for all y/R locations. Note that in the tip region, the values of δ^*, θ^* and H at y/R = 0.96 are much larger than values at y/R = 0.70 due to the higher transonic streamwise velocities.

Global Flow Features

Figures 9(a) - 9(d) and 10(a) - 10(d) are the static pressure and Mach contour fields for both airfoils at y/R = 0.96, 0.90, 0.80, 0.70. The free stream pressure and Mach contours in these figures are normalized to $\rho_\infty = 1$ and $M_\infty = 0.86$. These figures show that for both airfoils the shock position is nicely captured, and for the NACA-0012 the last 60% of the airfoil's upper surface suffers from flow separation, while for the CAST7-158, only the last 30% of the upper surface is separated. The longer separated region of the NACA-0012 contributes to larger unsteady pressure oscillations in the aft portion of the flow and in the near and far wake, and contributes to stronger noise propagation.

IV. CONCLUSIONS

The aerodynamic loads on a onebladed helicopter rotor in forward flight at transonic tip condition were calculated. The unsteady, three dimensional, time accurate, compressible Reynolds-averaged thin layer N-S equations are solved in an inertial coordinate system on a body conformed curvilinear grid of C-H topology. Detailed boundary layer and global numerical comparison of NACA-0012 symmetrical and CAST7-158 supercritical airfoils are made under identical forward flight conditions. It was shown that in all spanwise locations the method is capable of resolving the viscous layer, capturing the shock position, and predicting the overall flow field behavior.

The near future plans for the present method is to modify the inefficient C-H grid topology to that of either an 0-0 or 0-H topology and to extend the spatial accuracy of the scheme to higher orders to resolve the possible attenuation of propagating waves in the far field.

ACKNOWLEDGEMENTS

The author wishes to express his gratitude to Mr. Ralph Jolly of PRC-ATD for the assistance in the execution of the CAMRAD program.

REFERENCES

1. Johnson, W., "A Comprehensive Analytical Model of Rotorcraft Aerodynamics and Dynamics," Part I: Analysis Development, NASA TM-81182, AVRADCOM TR-80-A-5, 1980.
2. Agarwal, R. K., and Deese, J. E., "Euler Calculations for Flowfield of a Helicopter Rotor in Hover," J. Aircraft, V-24, N-4, Apr. 1987.
3. Maestrello, L., Badavi, F. F., and Noonan, K. W., "An Application of Active Surface Heating for Augmenting Lift and Reducing Drag of an Airfoil," NASA-TM-100563.
4. Isom, M. P., "Unsteady Subsonic and Transonic Potential Flow over Helicopter Rotor Blades," NASA-CR-2463, Oct. 1974.
5. Srinivasan, G. R., and McCroskey, W. J., "Navier-Stokes Calculations of Hovering Rotor Flowfields," AIAA-87-2628-CP, Monterey, Ca., Aug. 17-19, 1987.
6. Thomas, J. L., Taylor, S. L., and Anderson, W. K., "Navier-Stokes Computations of Vortical Flows over Low Aspect Ratio Wings," AIAA-87-0207, Reno, Nev., Jan. 12-15, 1987.
7. Van Leer, B., "Flux Vector Splitting for the Euler Equations," Lecture Notes in Physics, V-170, pp. 501-512, 1982.
8. Van Leer, B., "Towards the Ultimate Conservative Difference Scheme V. A Second Order Sequel to Gudonov's Method," J. of Computational Physics, V-32, pp. 101-136, 1979.
9. Beam, R., and Warming, R., "An Implicit Finite Difference Algorithm for Hyperbolic Systems in Conservative Law Form," J. of Computational Physics, V-22, pp. 87, 1976.
10. Baldwin, B. S., and Lomax, H., "Thin Layer Approximation and Algebraic Model for Separated Turbulent Flows," AIAA-78-257, Jan. 1978.
11. Thomas, J. L, and Salas, M. D., "Far Field Boundary Conditions for Transonic Lifting Solutions to the Euler Equations," AIAA-85-0020, Reno, Nev., Jan. 14-17, 1985.
12. McCroskey, W. J., Baeder, J. D., and Bridgeman, J. D., "Calculation of Helicopter Airfoil Characteristics for High Tip Speed Applications," presented at the 41st Annual Forum of AHS, Ft. Worth, Tex., May 1985.

y/R	(CAST7-158) c_l	(NACA-0012) c_l	(CAST7-158) c_{d_p}	c_{d_f}	c_d	(NACA-0012) c_{d_p}	c_{d_f}	c_d
0.96	1.0602	0.5552	0.05871	0.00112	0.05983	0.03239	0.00104	0.03343
0.90	1.0241	0.5164	0.05196	0.00111	0.05307	0.02776	0.00105	0.02881
0.80	0.9151	0.3979	0.03455	0.00110	0.03565	0.01625	0.00108	0.01733
0.70	0.7910	0.2605	0.01852	0.00109	0.01961	0.00836	0.00111	0.00947

Table 1 - Lift and drag calculations based on thin layer N-S computations.

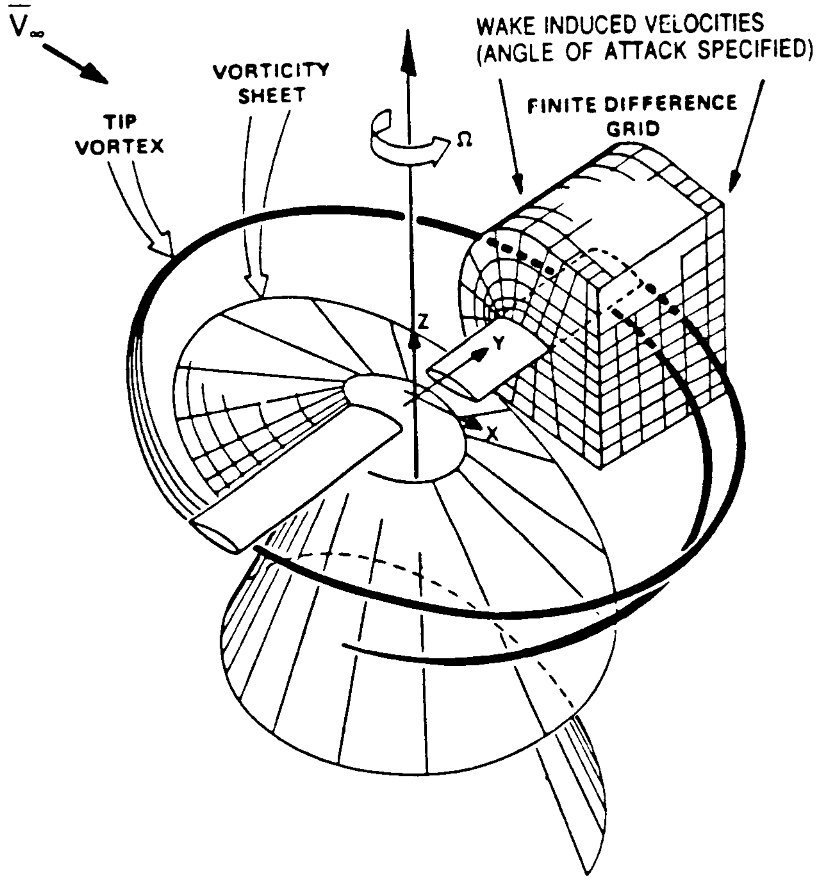

Fig.1 - Wake modeling by an angle of attack approach

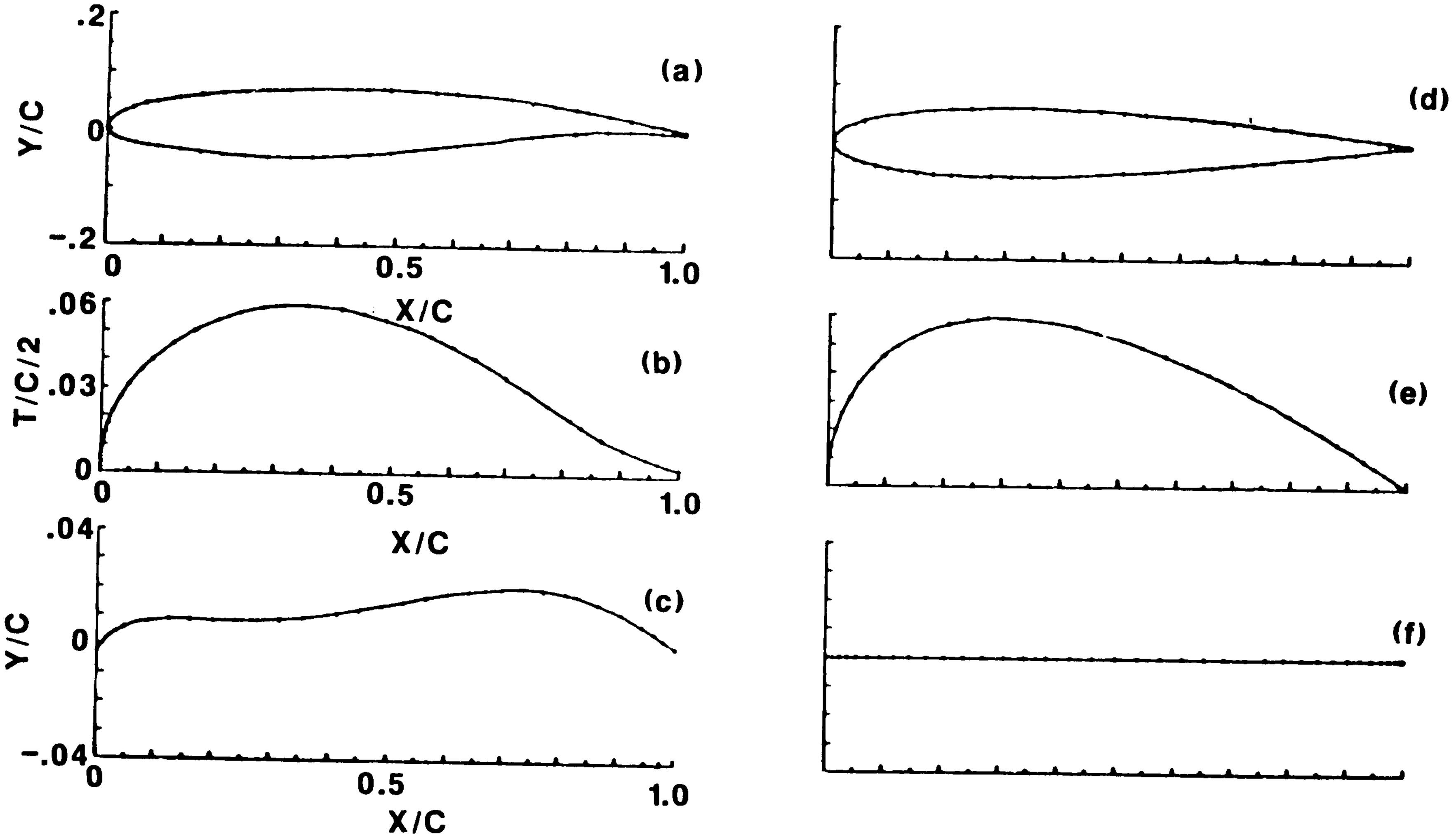

Fig.2 - CAST7-158 geometrical(a), half thickness(b), camber(c); NACA-0012 geometrical(d), half thickness(e), camber(f) distributions

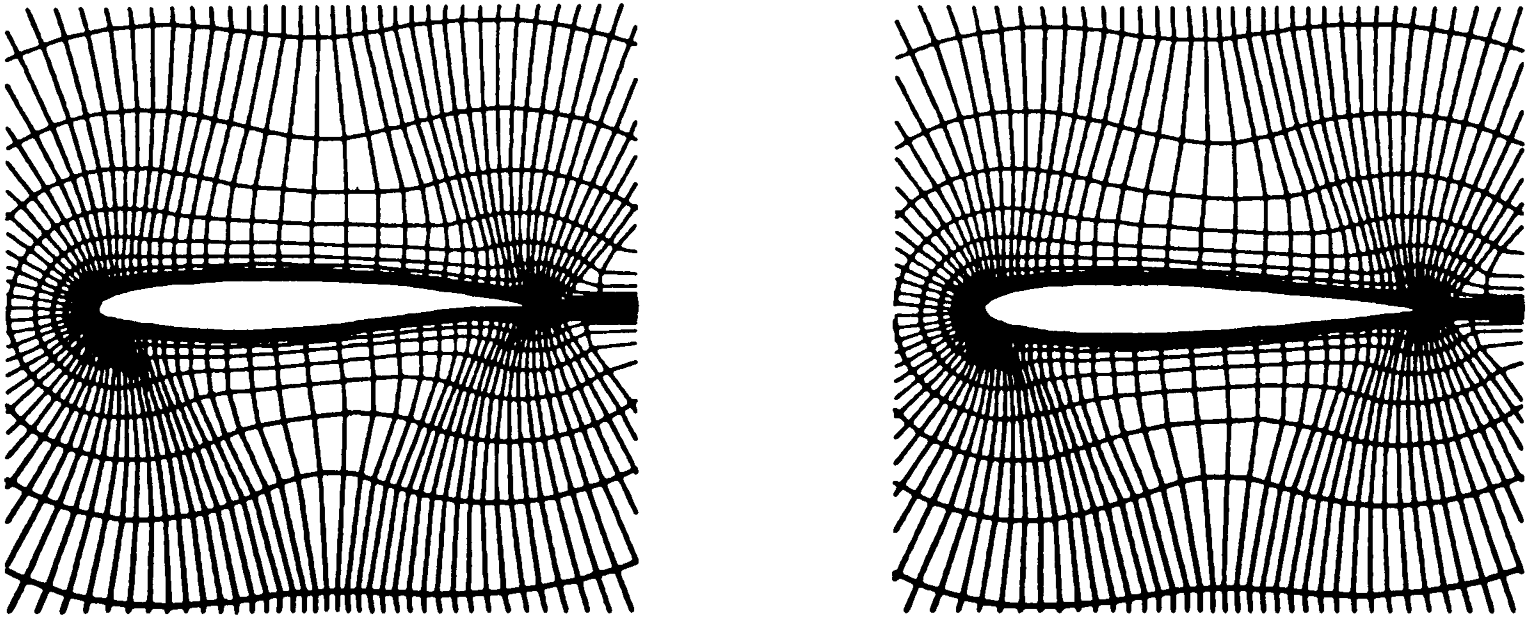

CAST7-158 Grid

NACA-0012 Grid

Fig.3 - Partial view of the C-plane of the C-H grid block for CAST7-158 and NACA-0012 airfoils

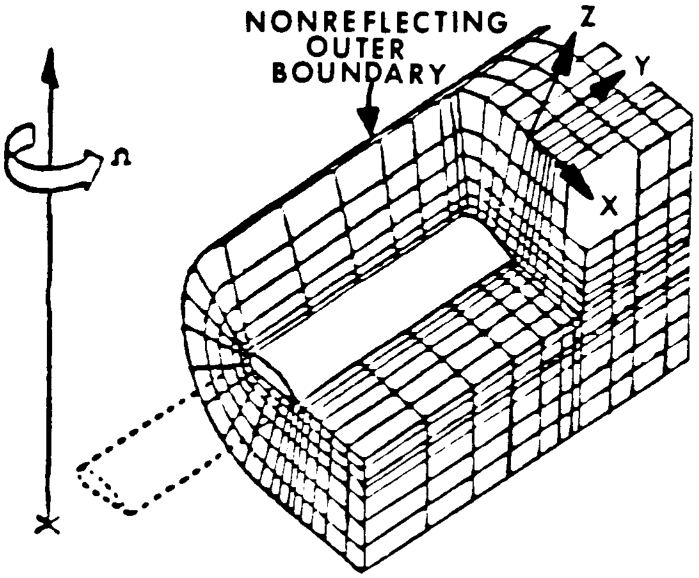

Fig.4 - Grid and boundary conditions for a rotor blade computations

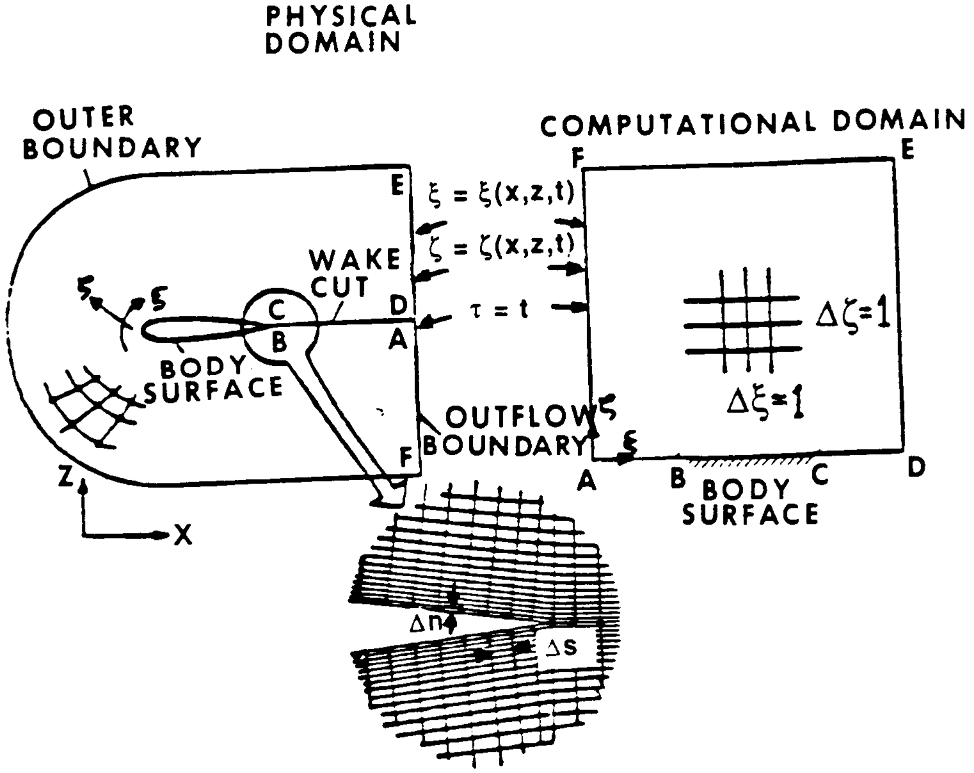

Fig.5 - Physical and transformed computational planes for the C-grid

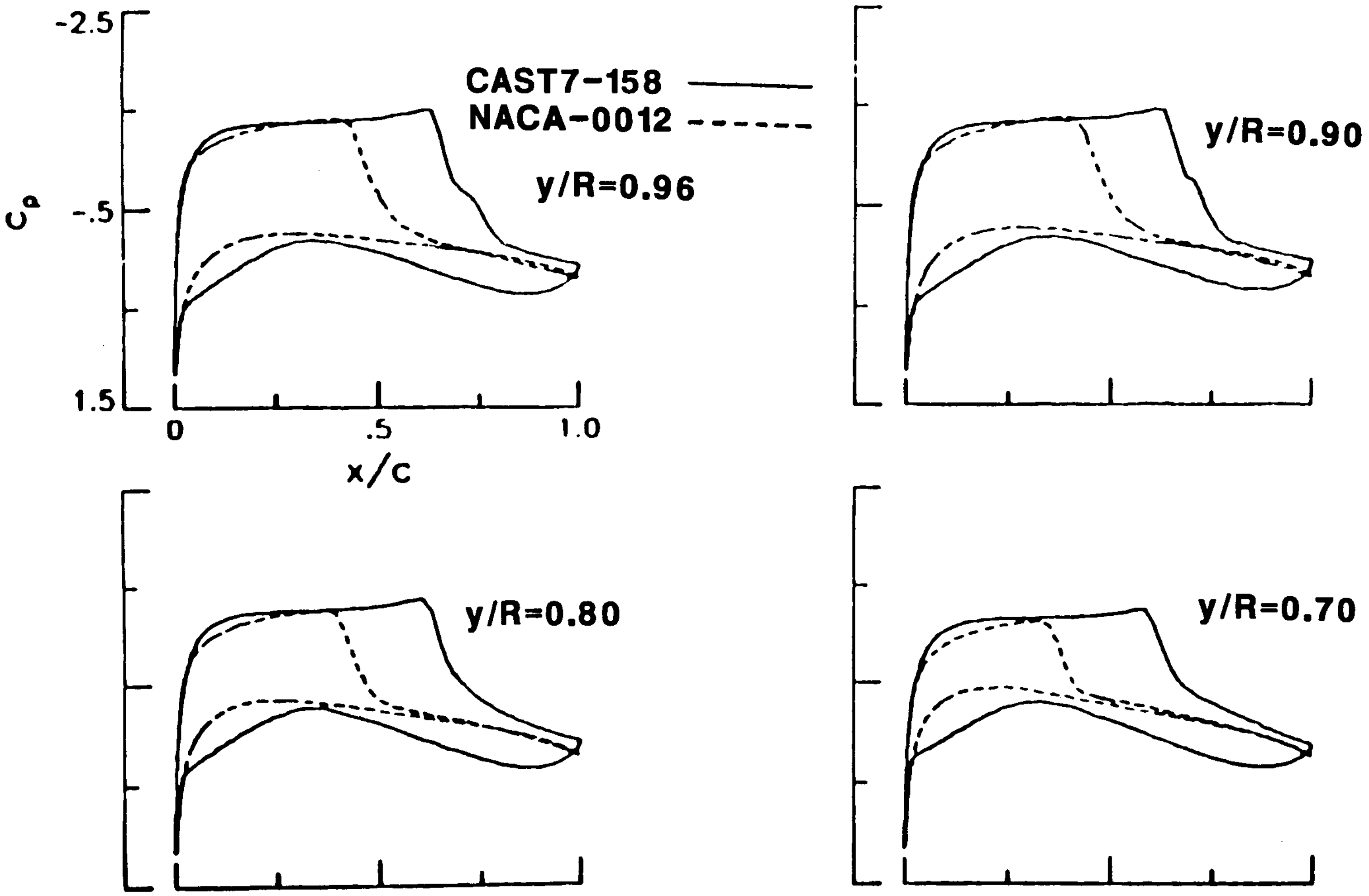

Fig.6 - Computed surface pressure distributions for CAST7-158 and NACA-0012 airfoils

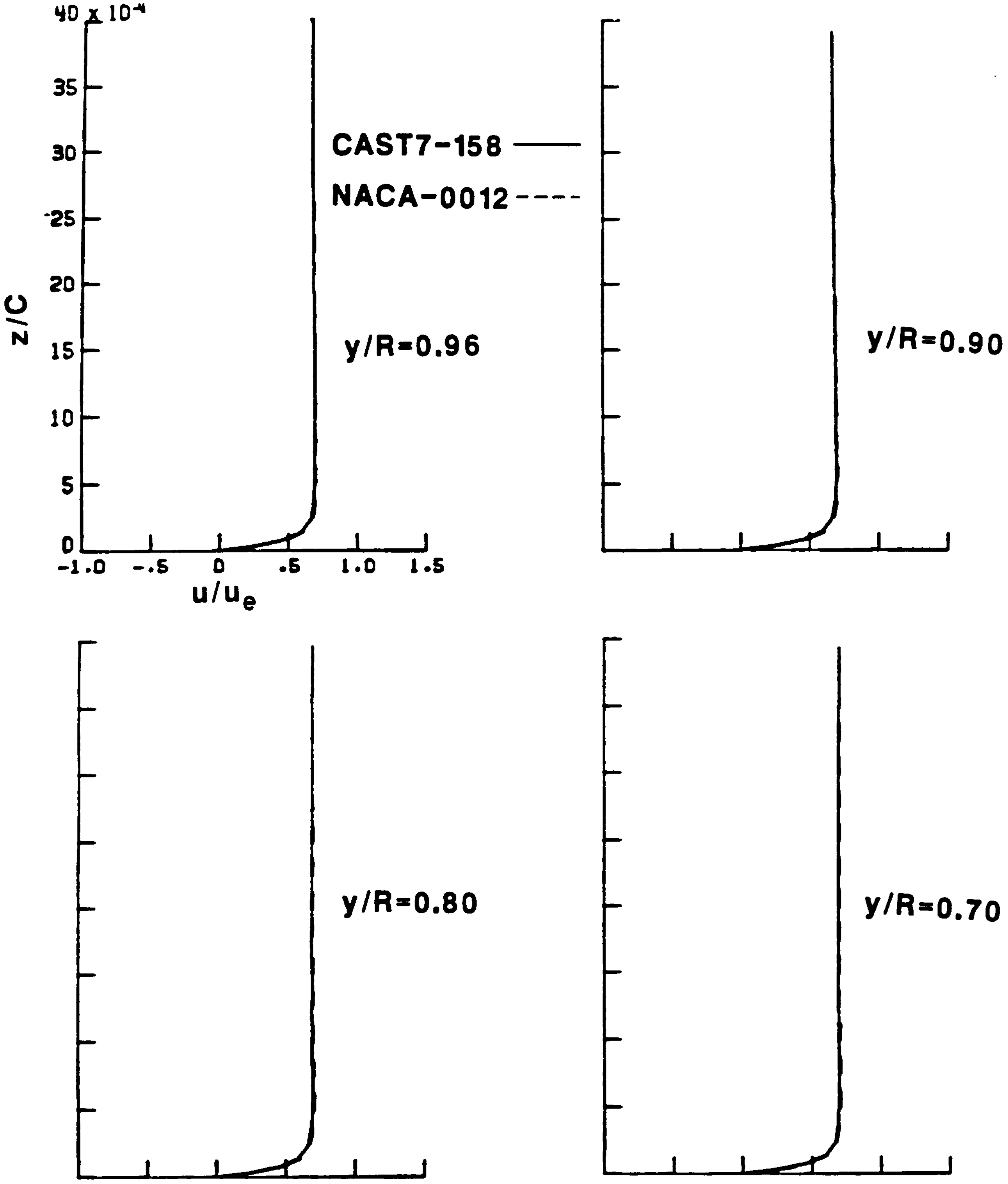

Fig.7(a) - Computed velocity profiles at x/c=0.01

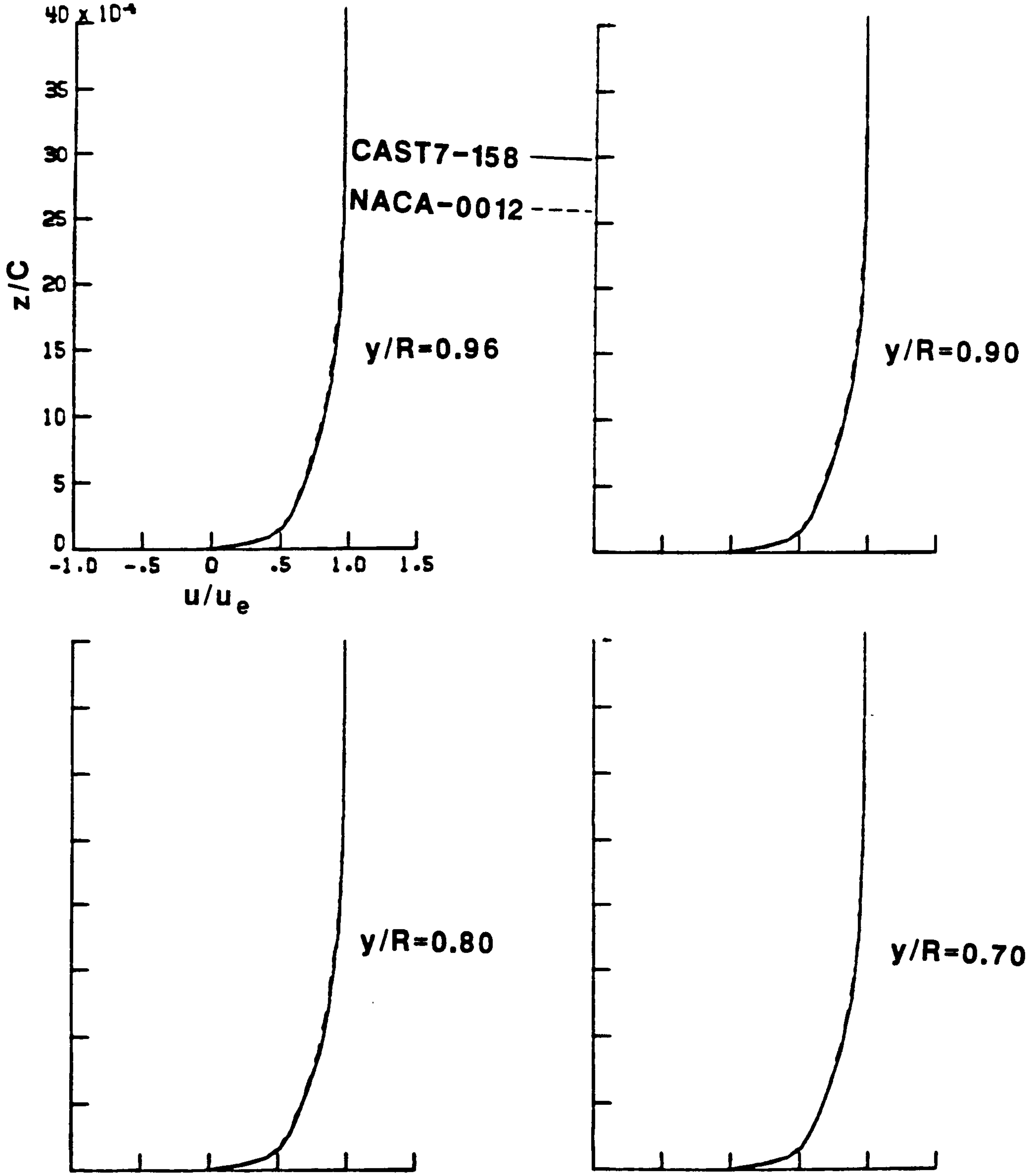

Fig.7(b) - Computed velocity profiles at x/c=0.10

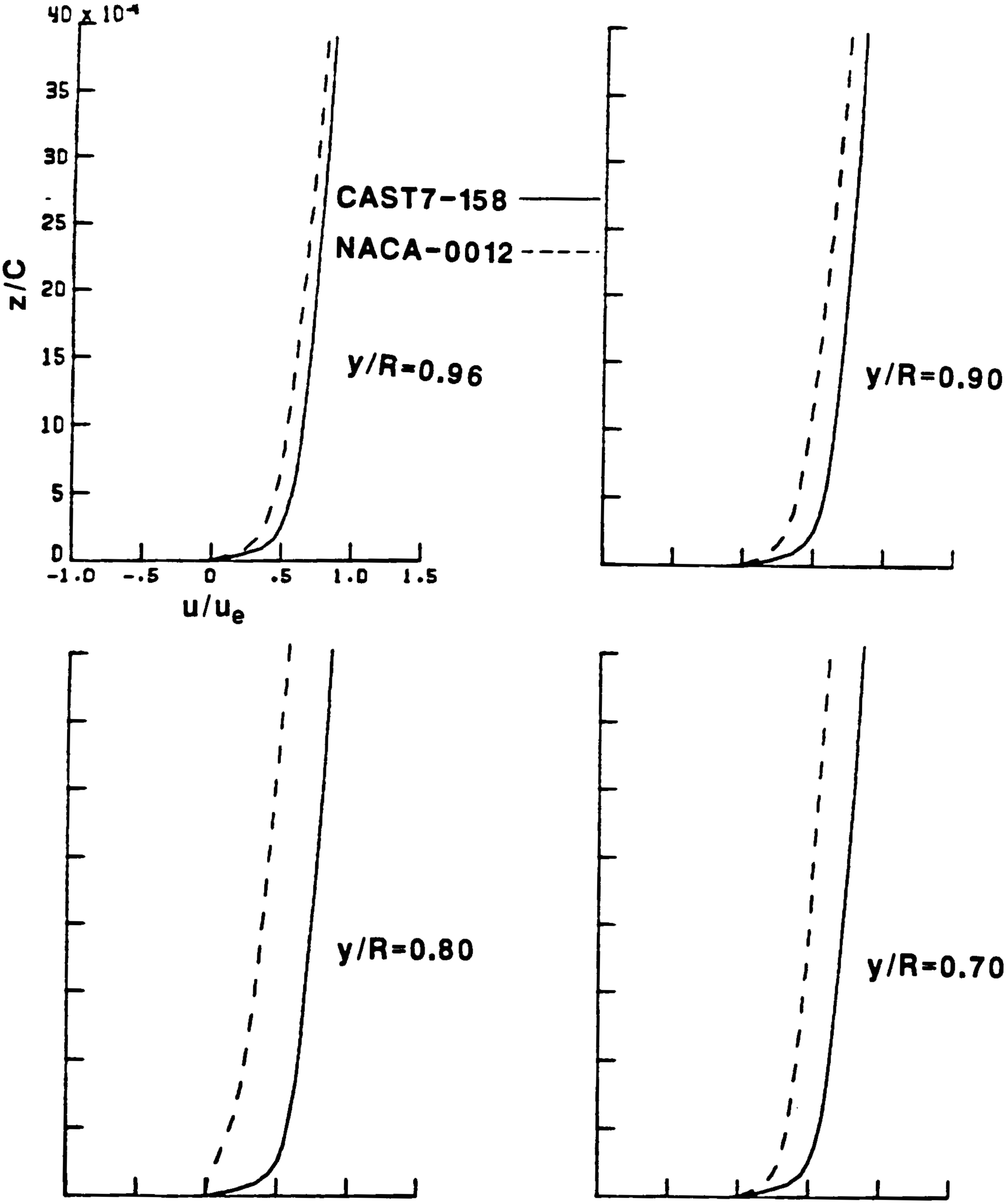

Fig.7(c) - Computed velocity profiles at x/c=0.44

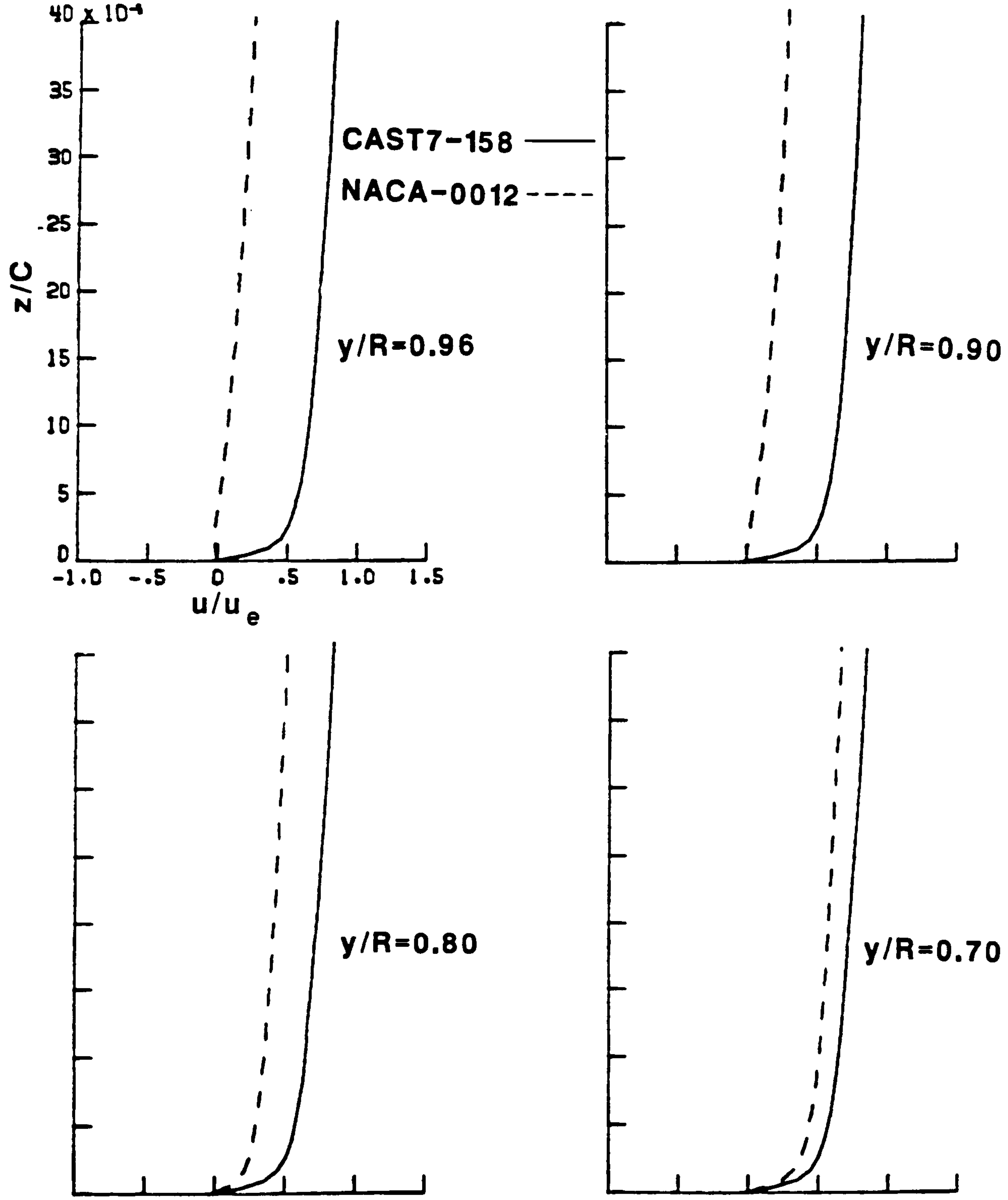

Fig.7(d) - Computed velocity profiles at x/c=0.57

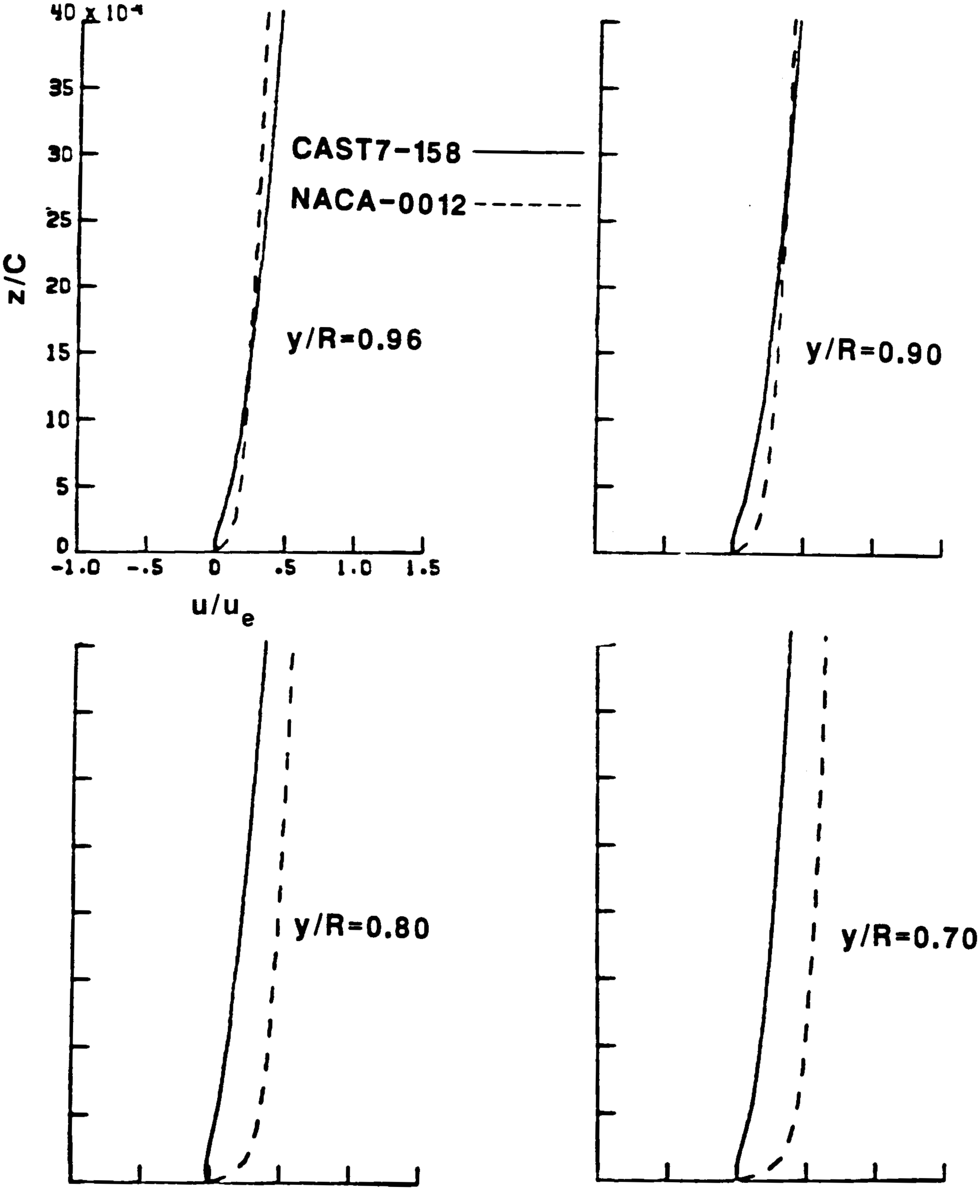

Fig.7(e) - Computed velocity profiles at x/c=0.67

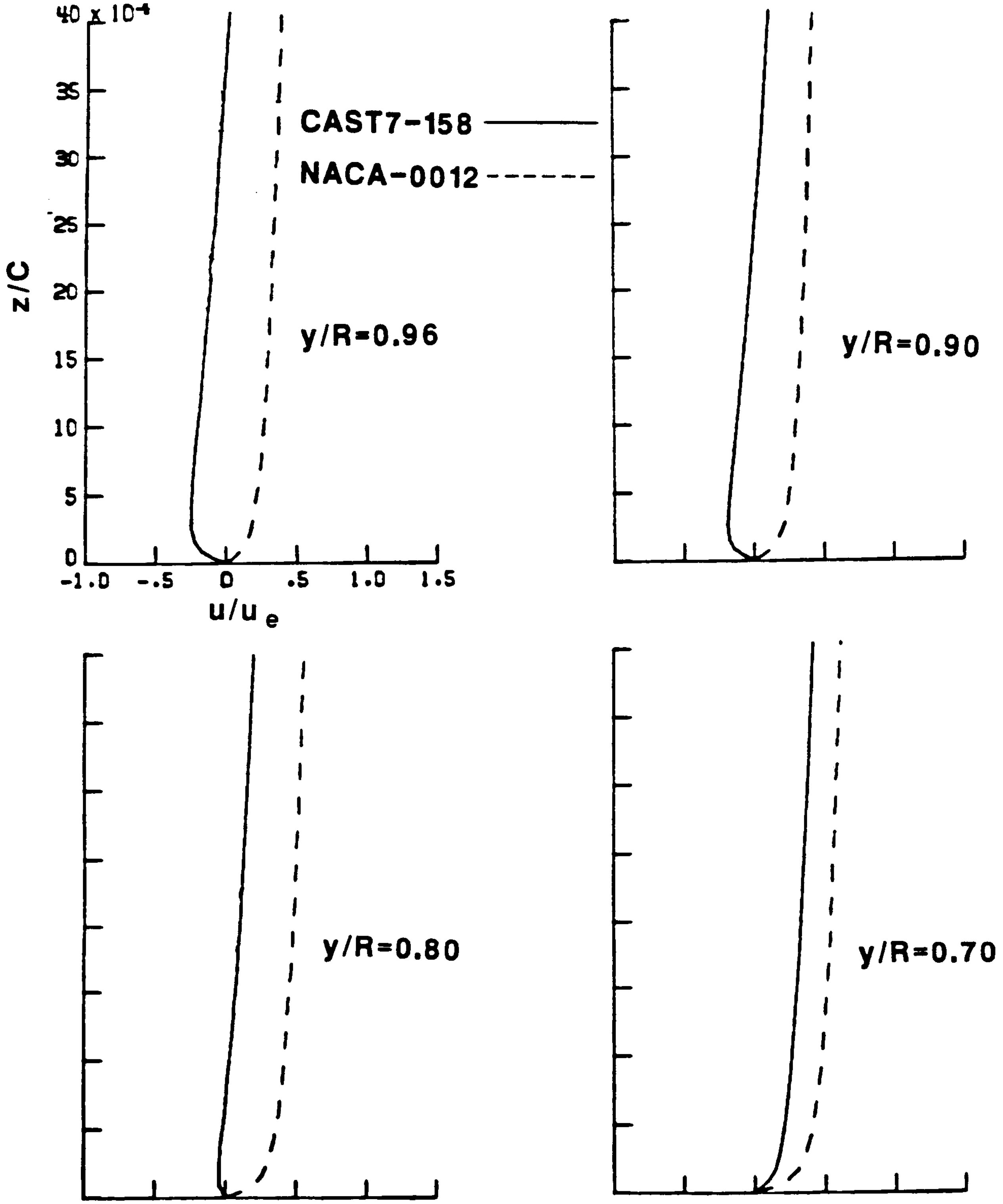

Fig.7(f) - Computed velocity profiles at x/c=0.75

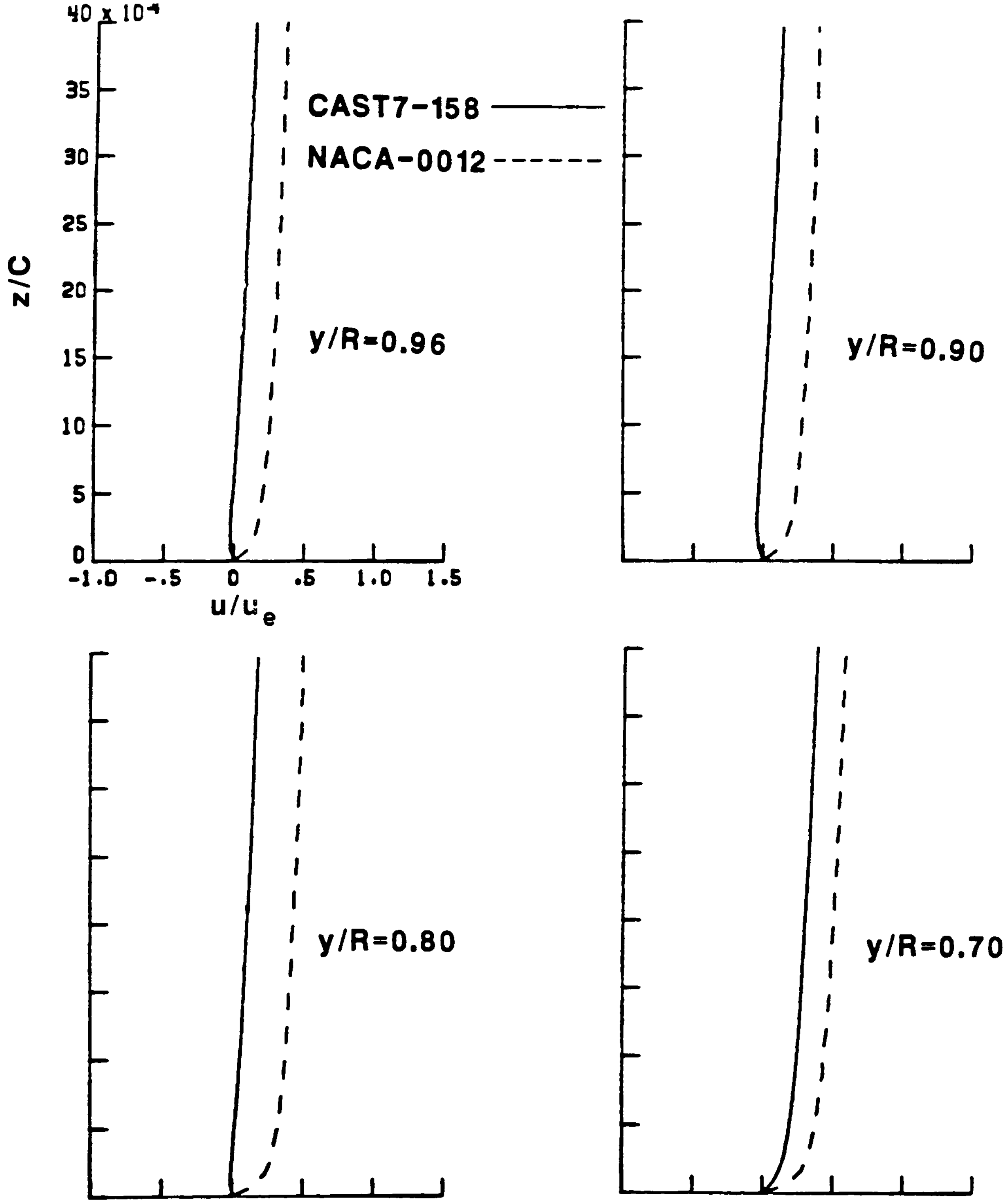

Fig.7(g) - Computed velocity profiles at x/c=0.86

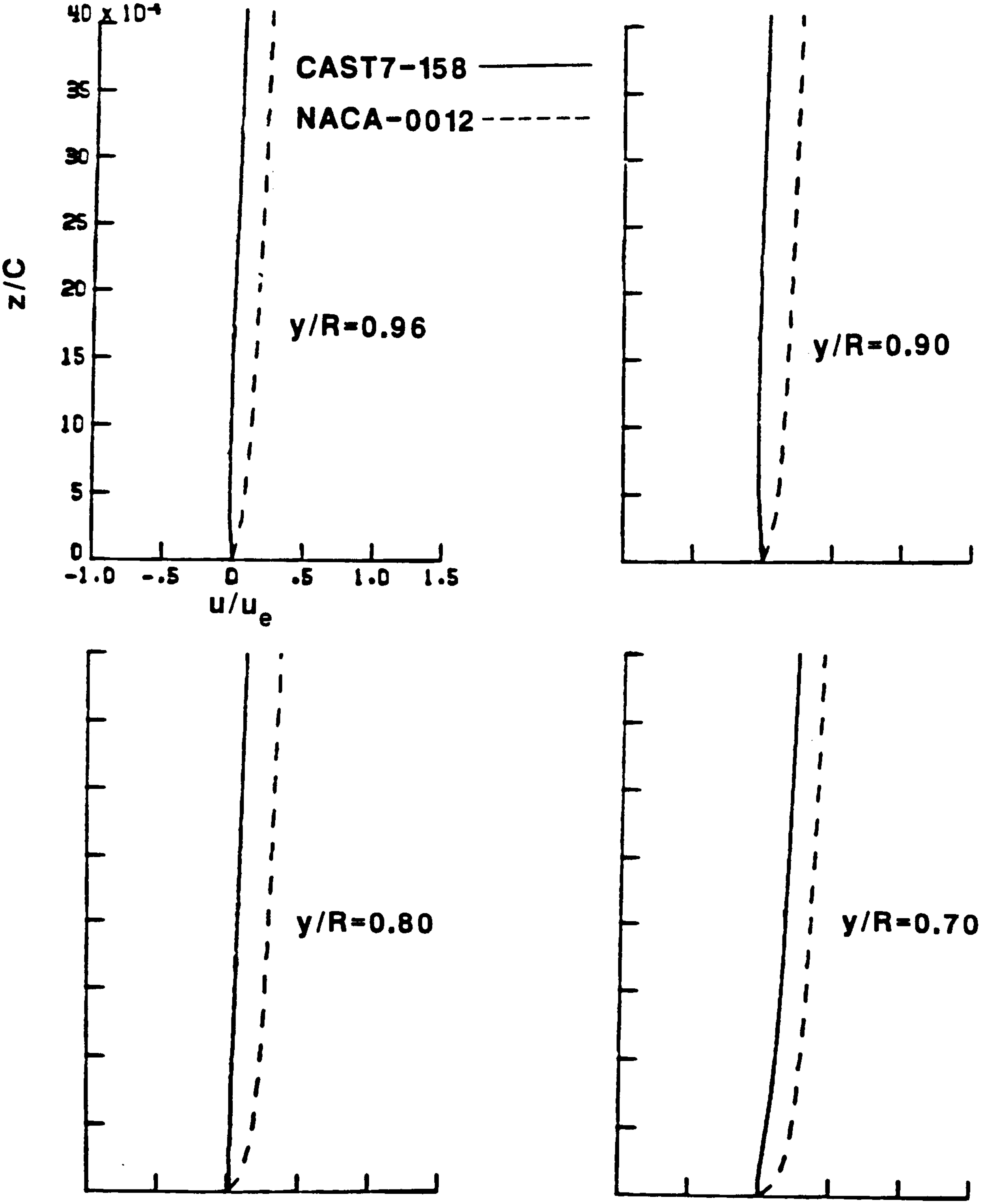

Fig.7(h) - Computed velocity profiles at x/c=0.99

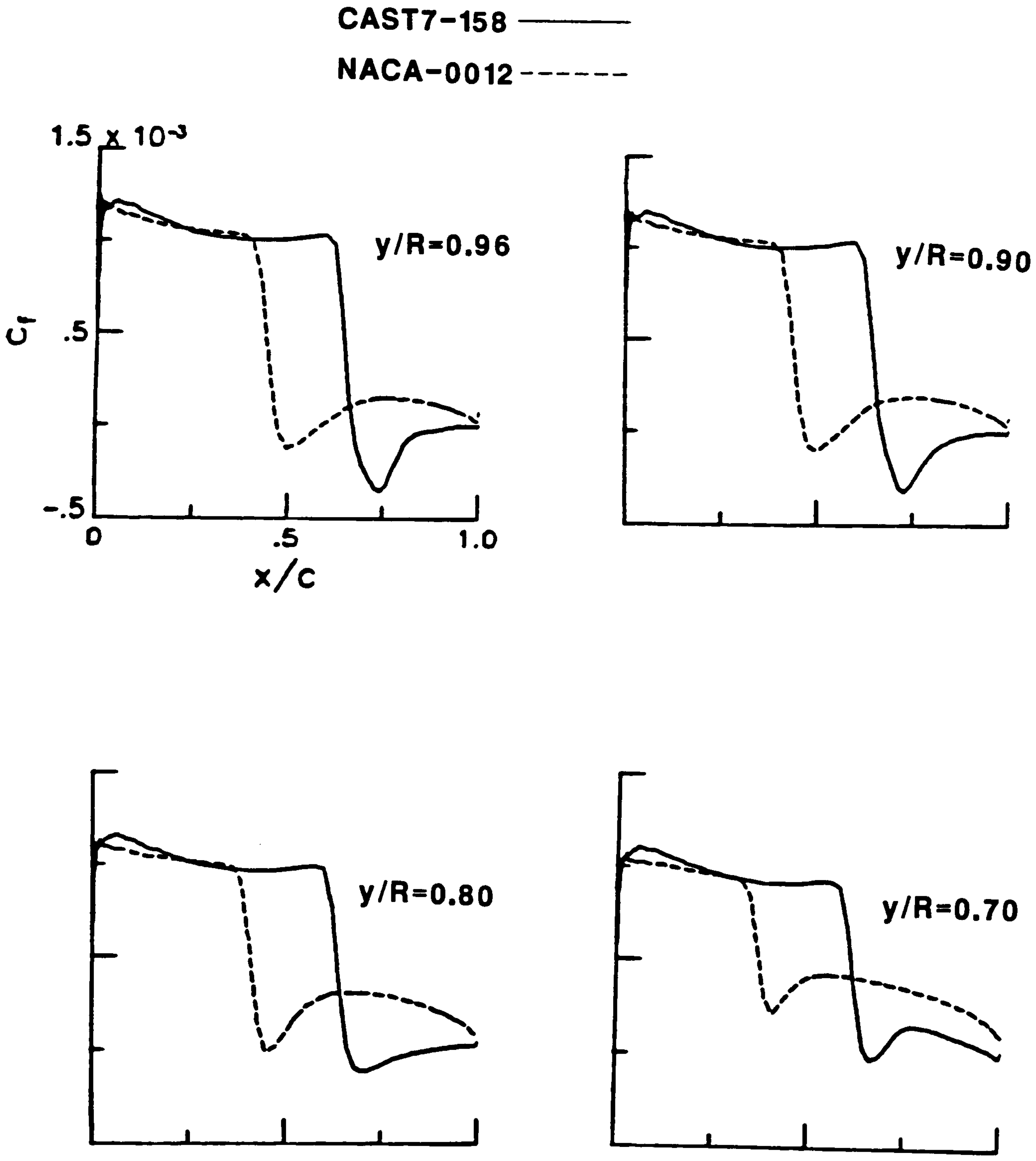

Fig.8(a) - Computed skin friction profiles for CAST7-158 and NACA-0012 airfoils

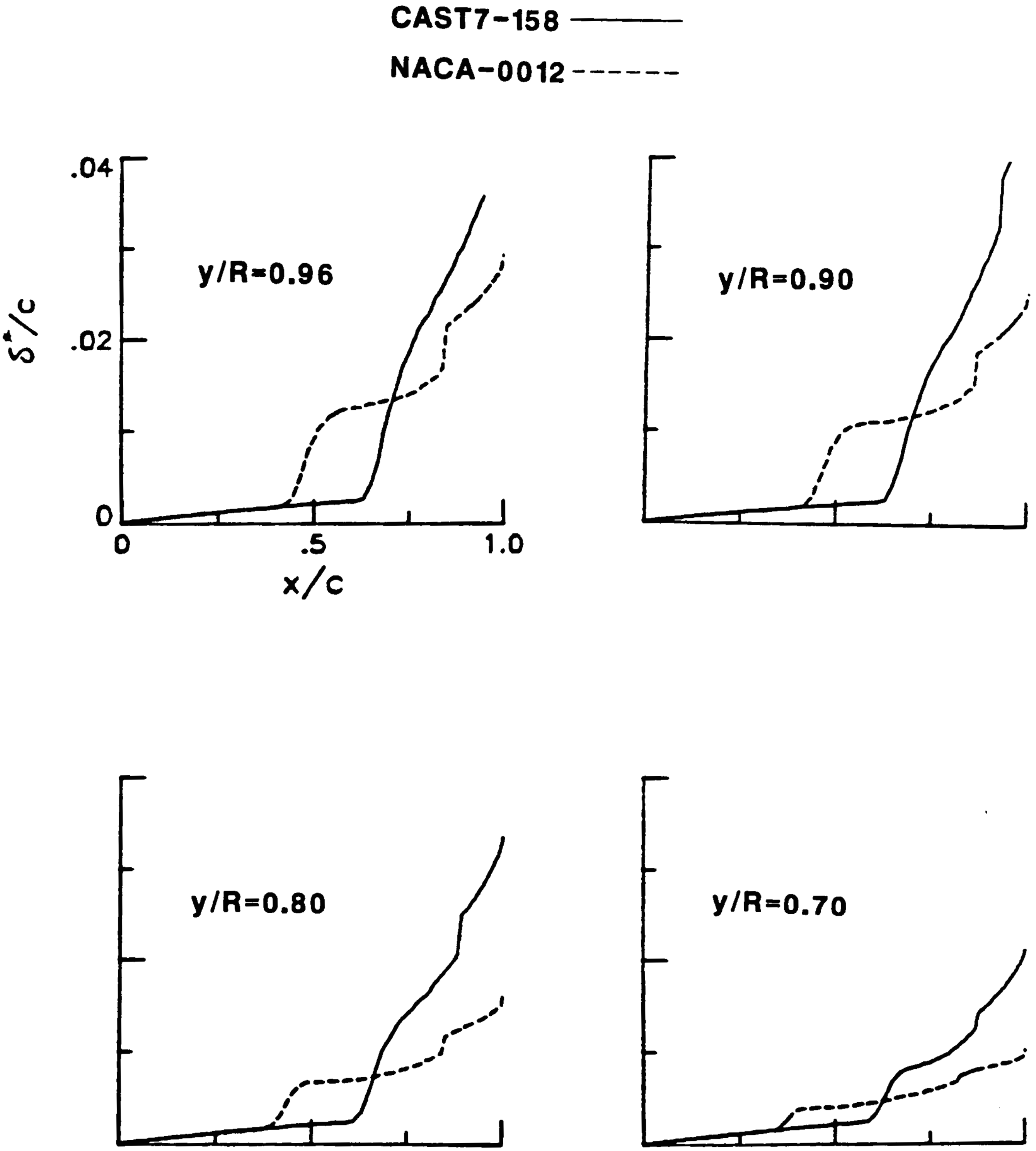

Fig.8(b) - Computed displacement thickness profiles for CAST7-158 and NACA-0012 airfoils

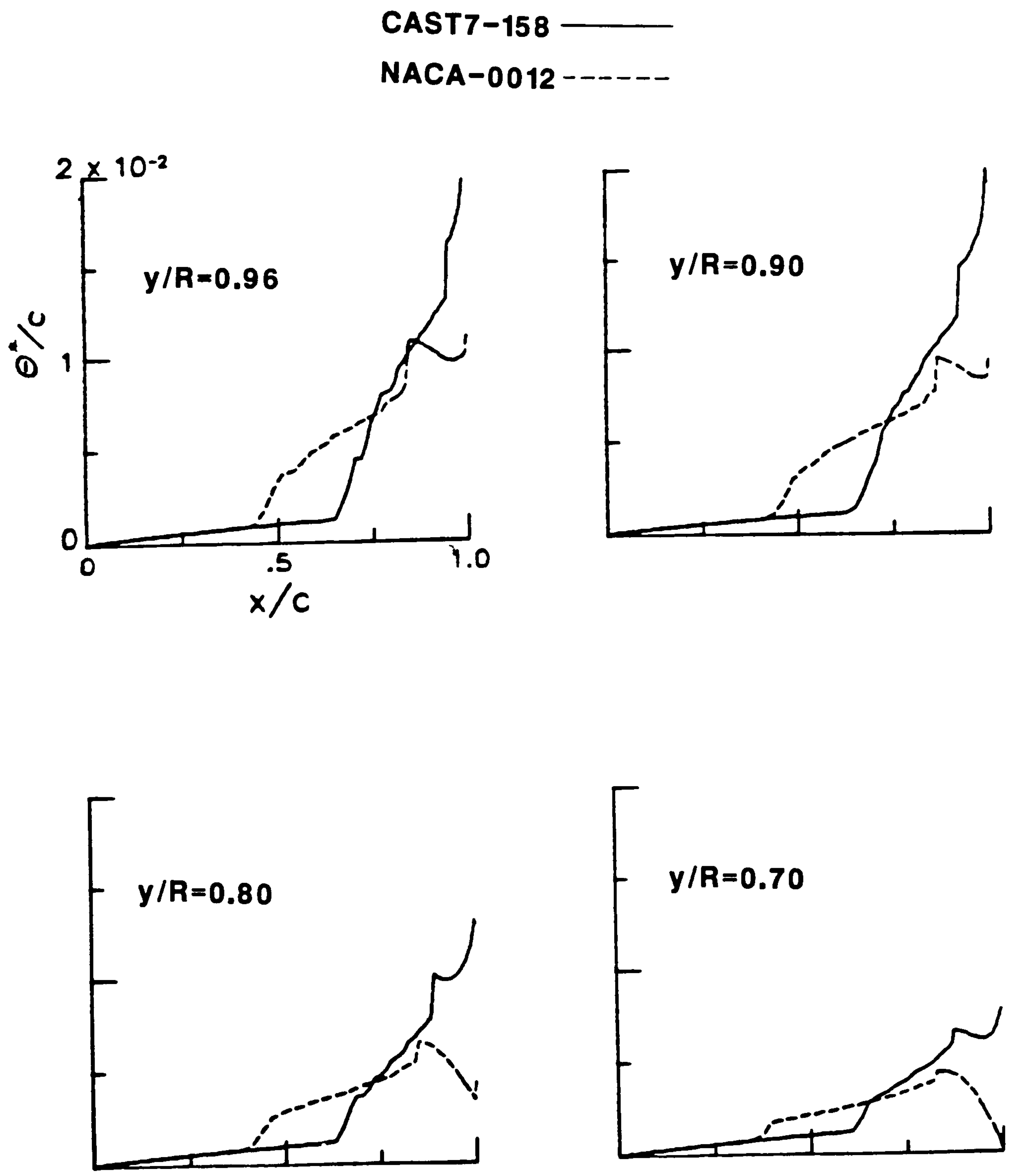

Fig.8(c) - Computed momentum thickness profiles for CAST7-158 and NACA-0012 airfoils

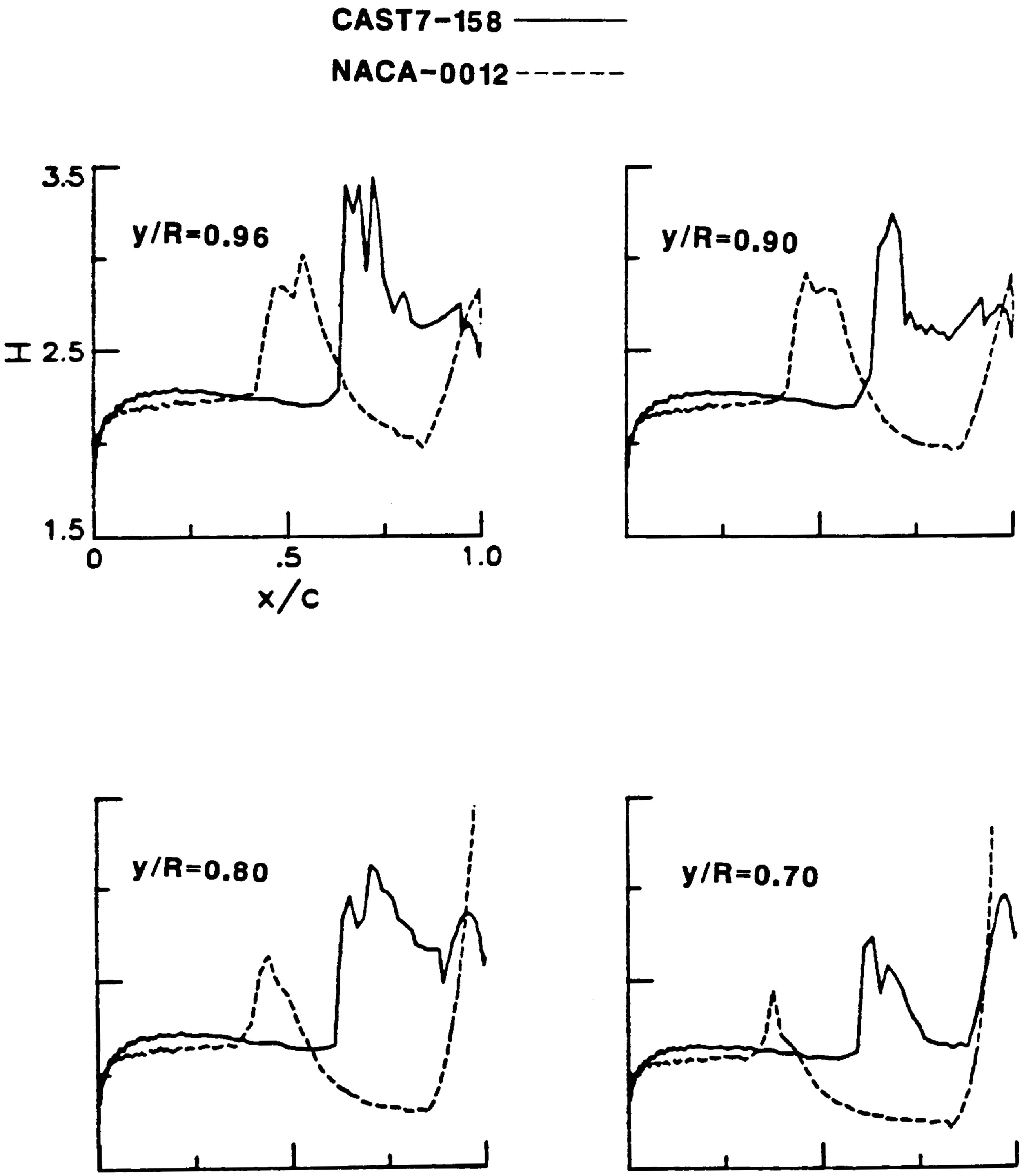

Fig.8(d) - Computed shape factor profiles for CAST7-158 and NACA-0012 airfoils

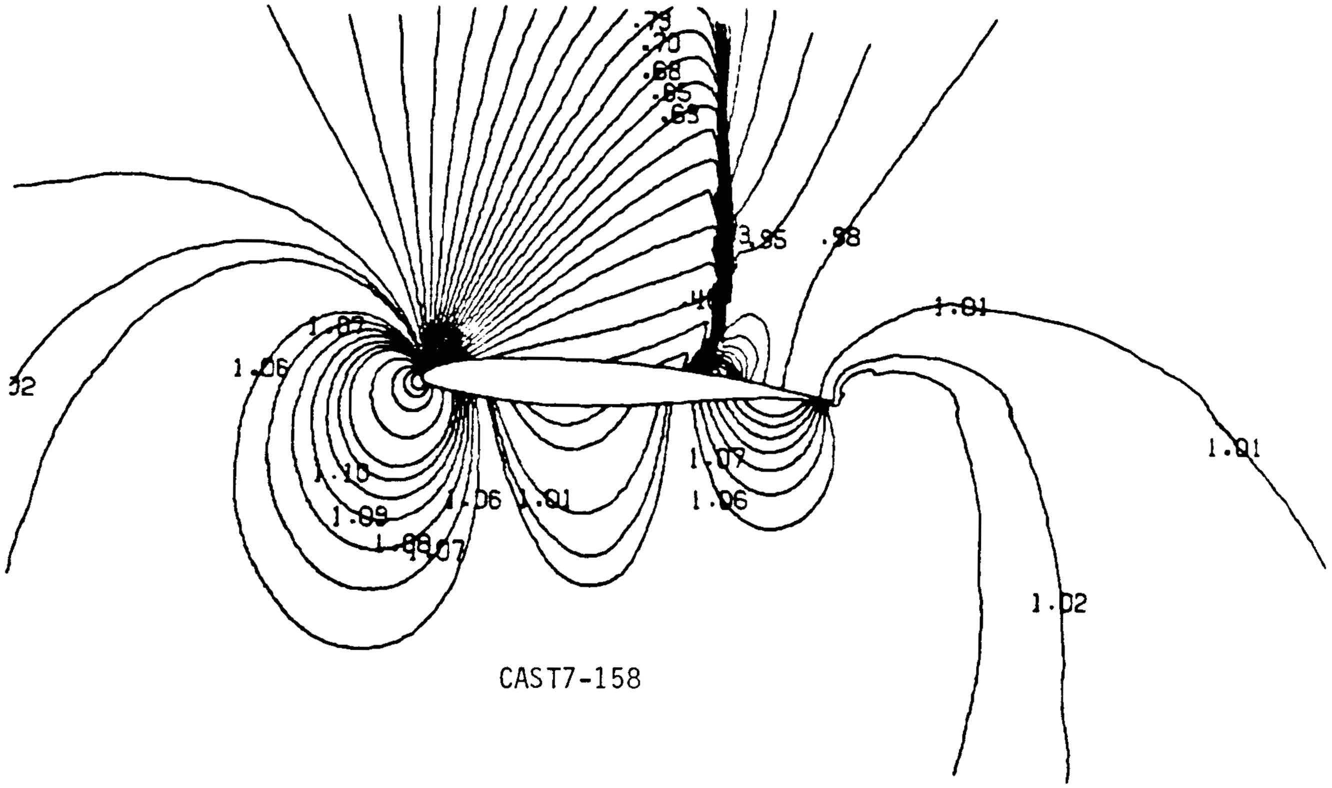

CAST7-158

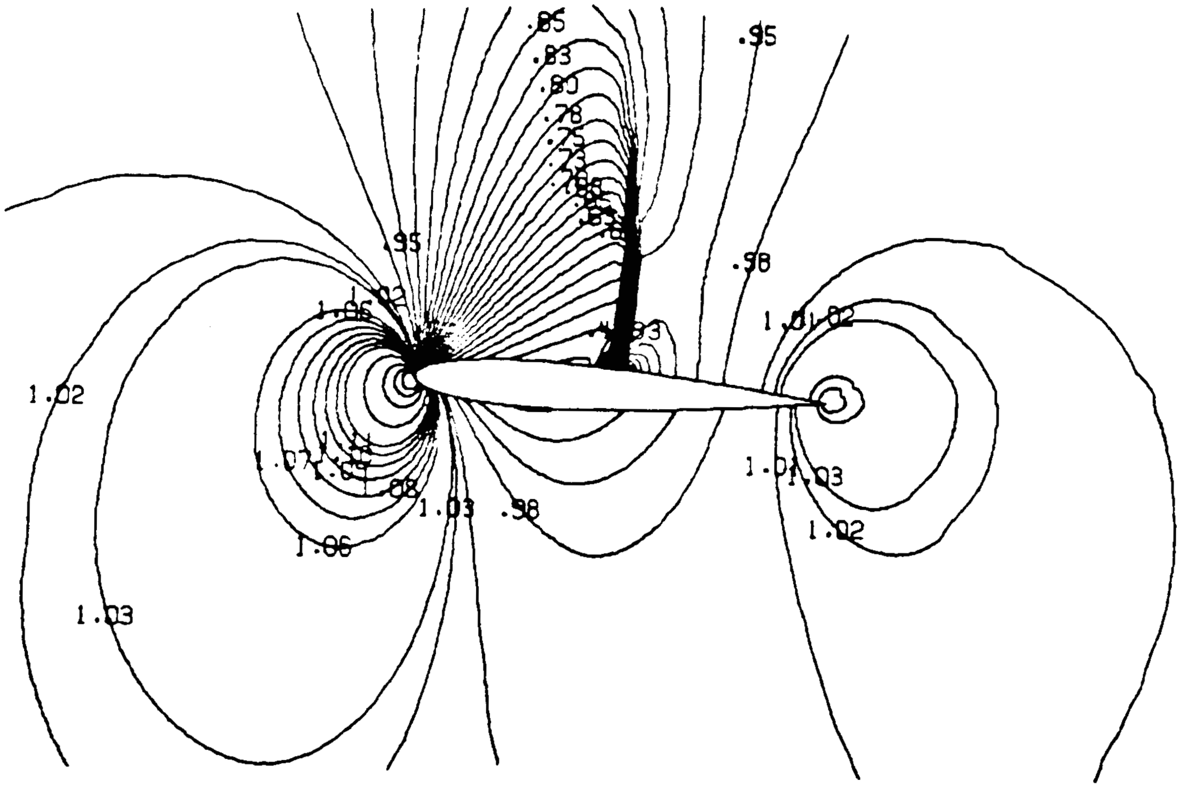

NACA-0012

Fig.9(a) - Static pressure contours for CAST7-158 and NACA-0012 at y/R=0.96

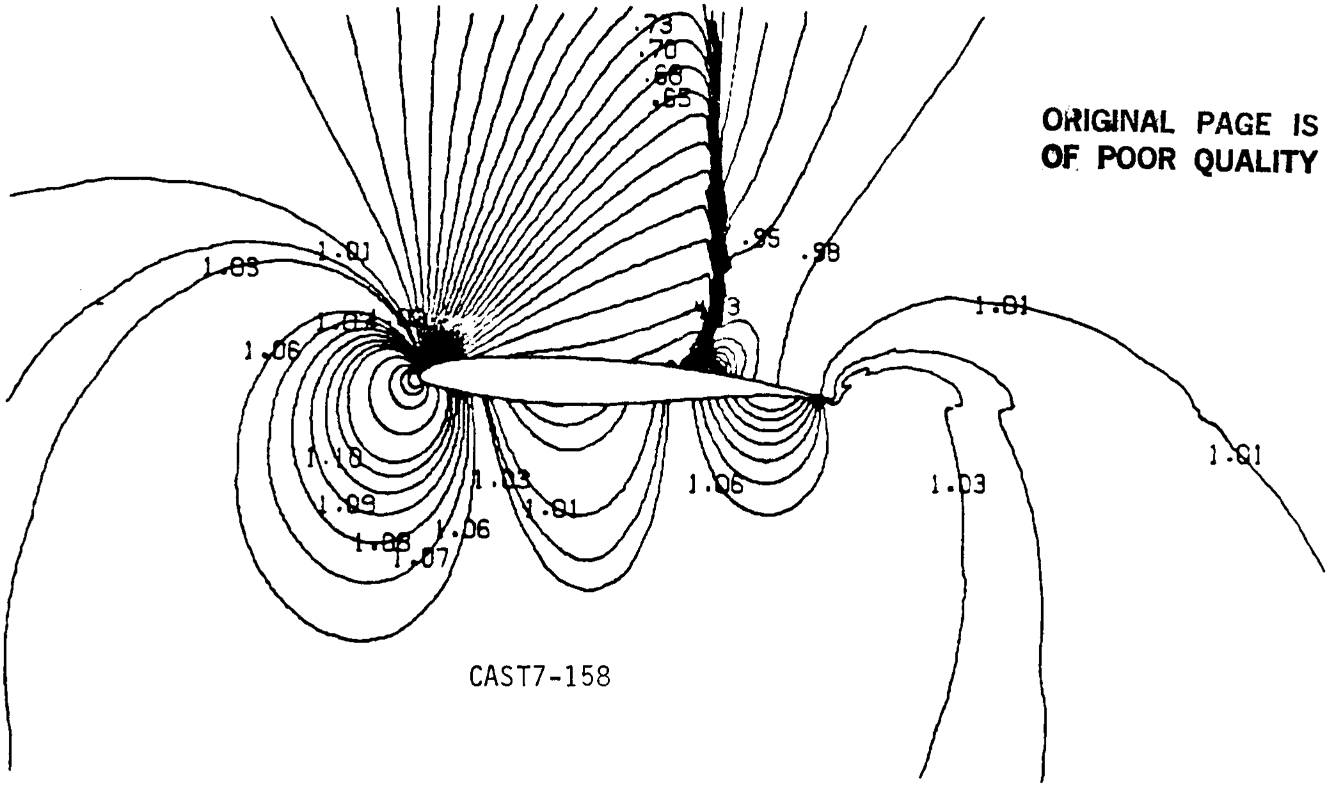

CAST7-158

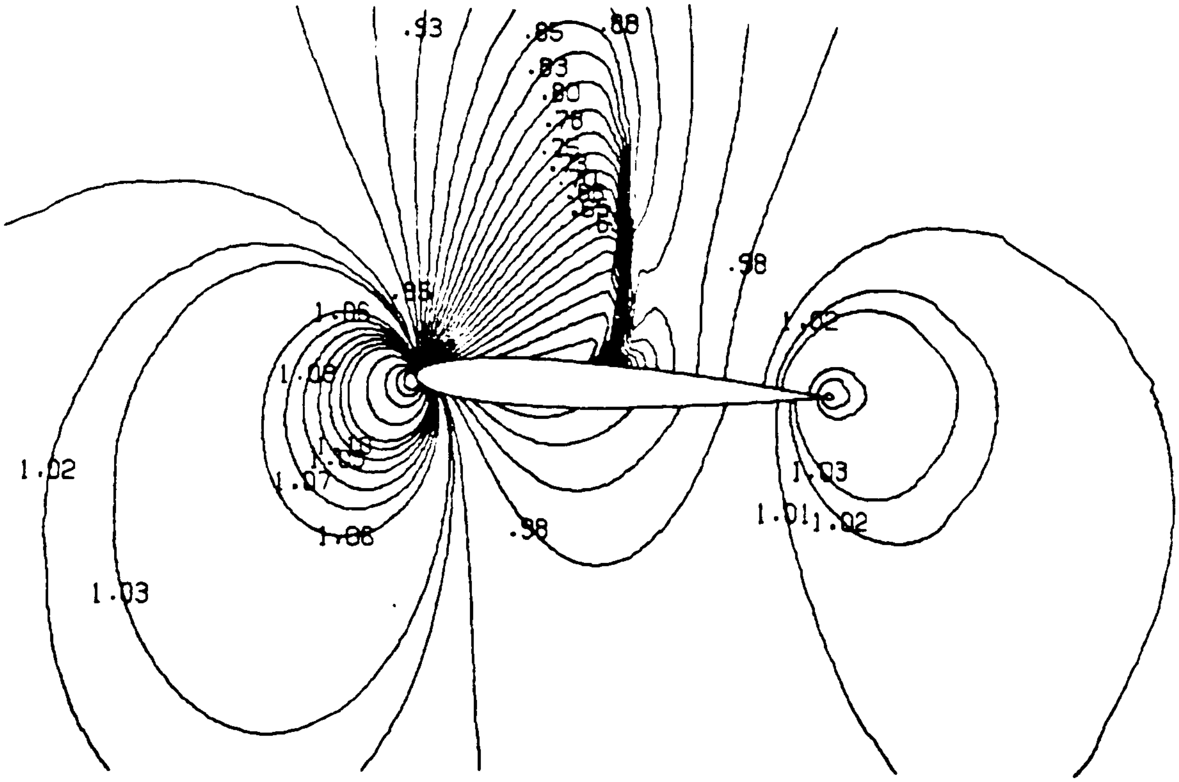

NACA-0012

Fig.9(b) - Static pressure contours for CAST7-158 and NACA-0012 at y/R=0.90

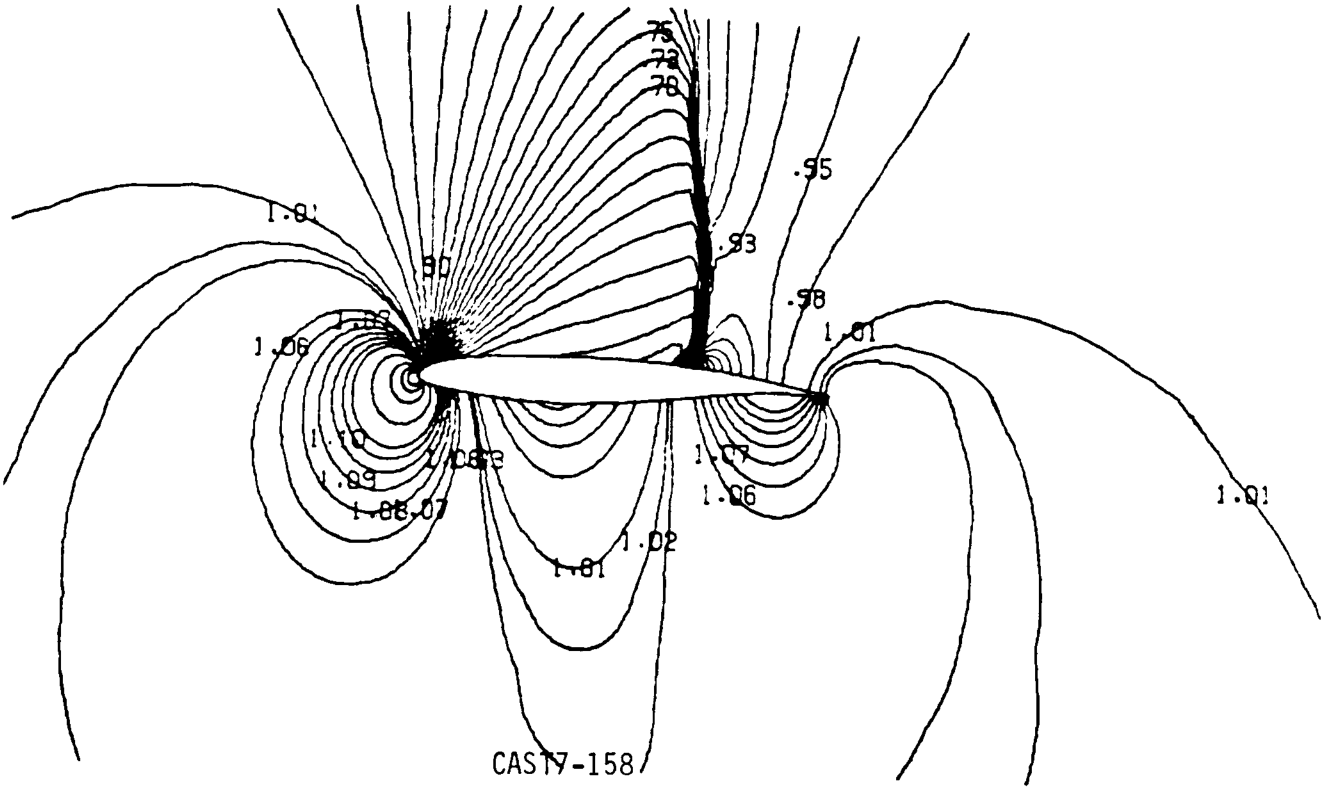

CAST7-158

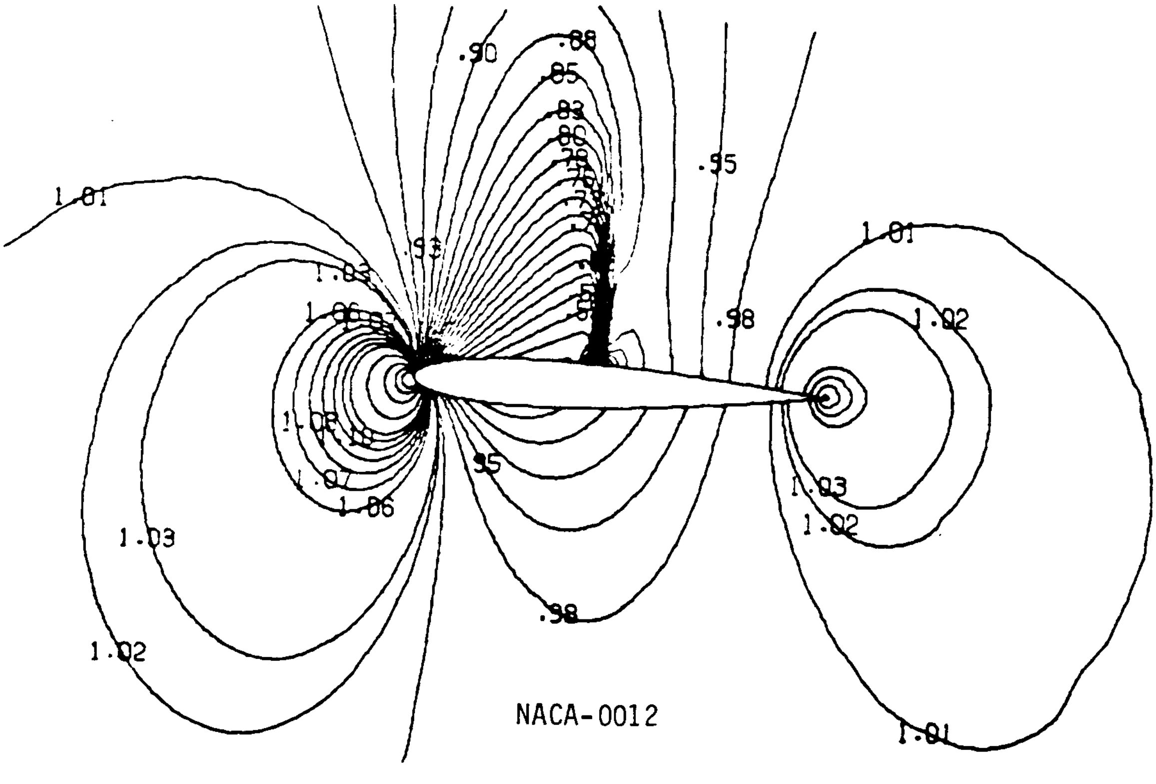

NACA-0012

Fig.9(c) - Static pressure contours for CAST7-158 and NACA-0012 at y/R=0.80

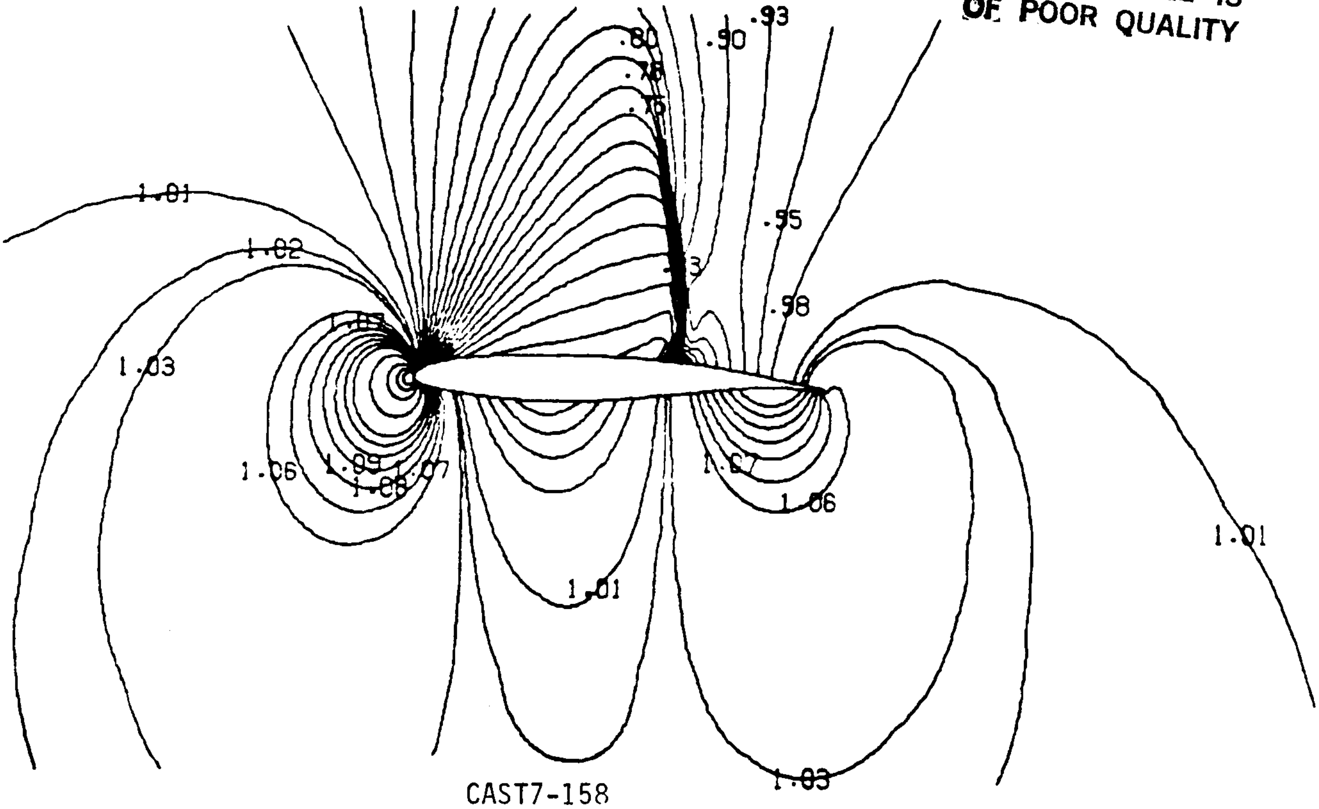

CAST7-158

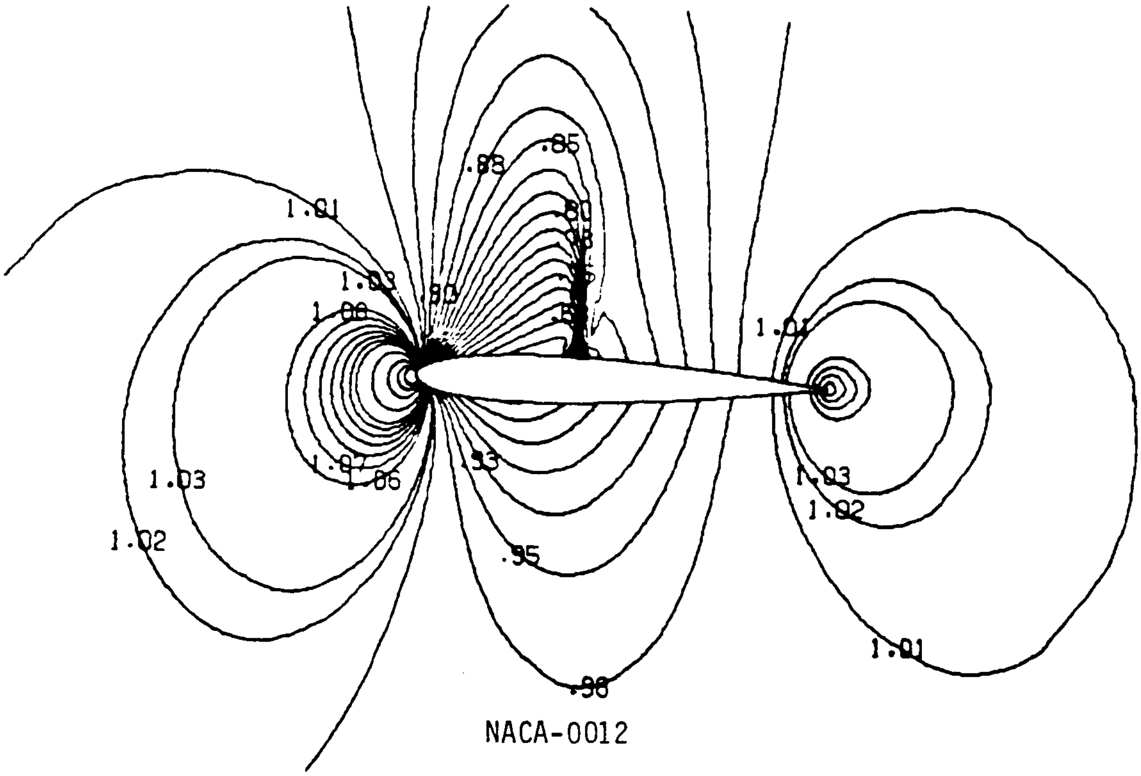

NACA-0012

Fig.9(d) - Static pressure contours for CAST7-158 and NACA-0012 at y/R=0.70

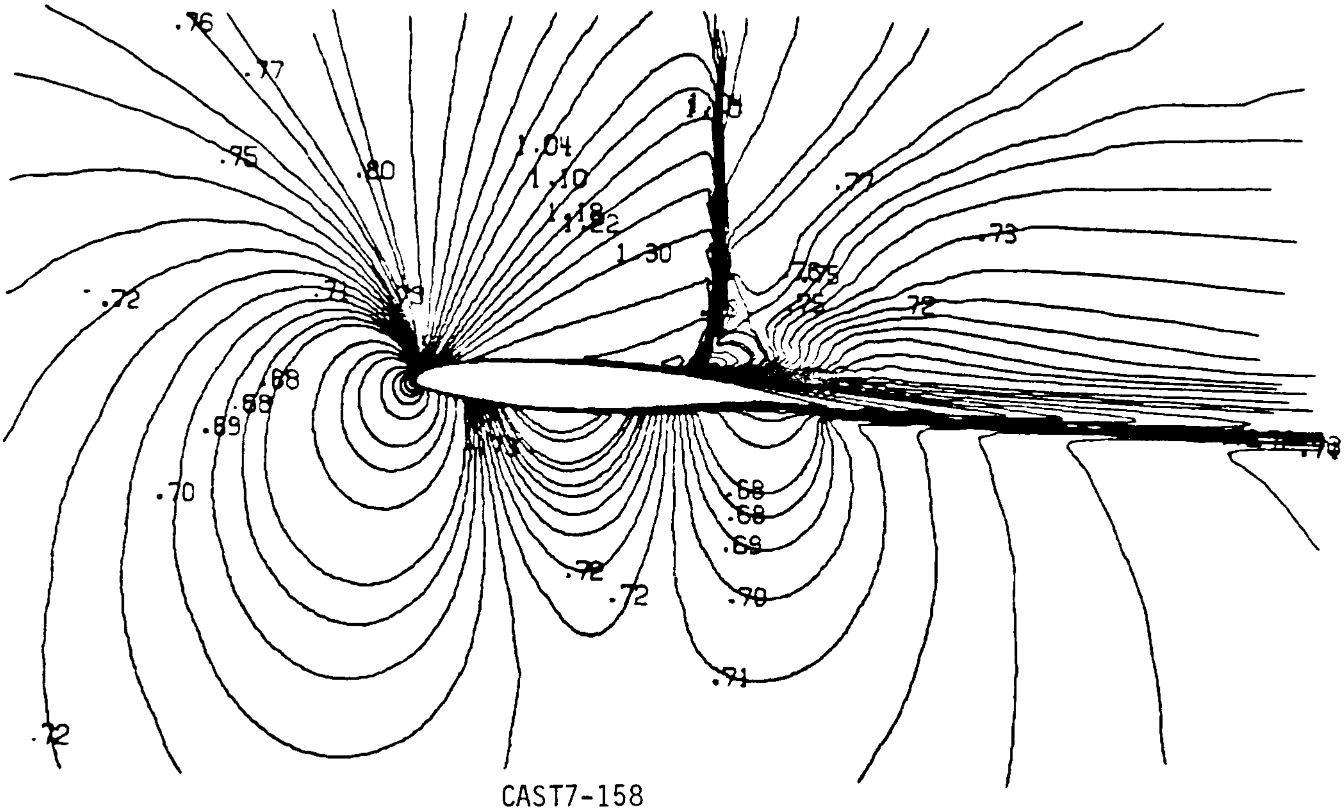

CAST7-158

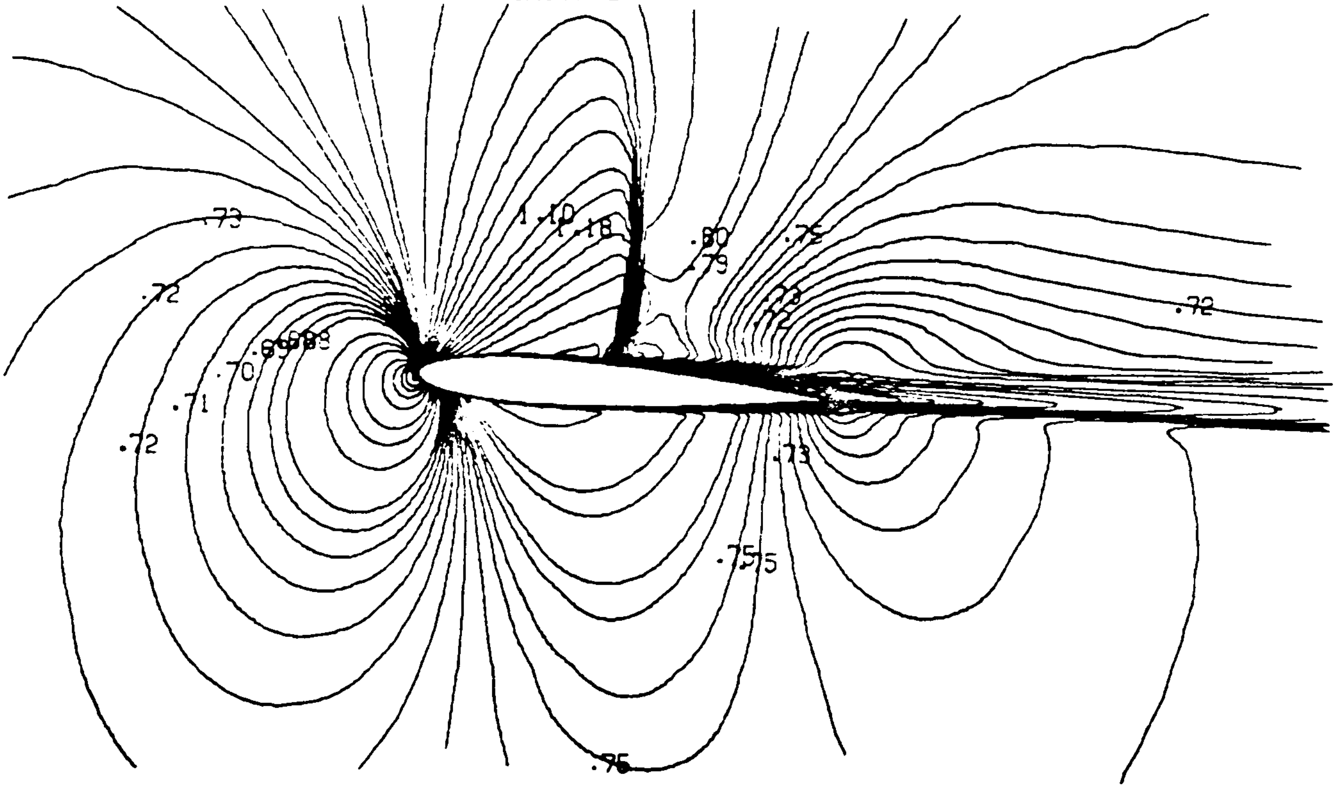

NACA-0012

Fig.10(a) - Mach contours for CAST7-158 and NACA-0012 at y/R=0.96

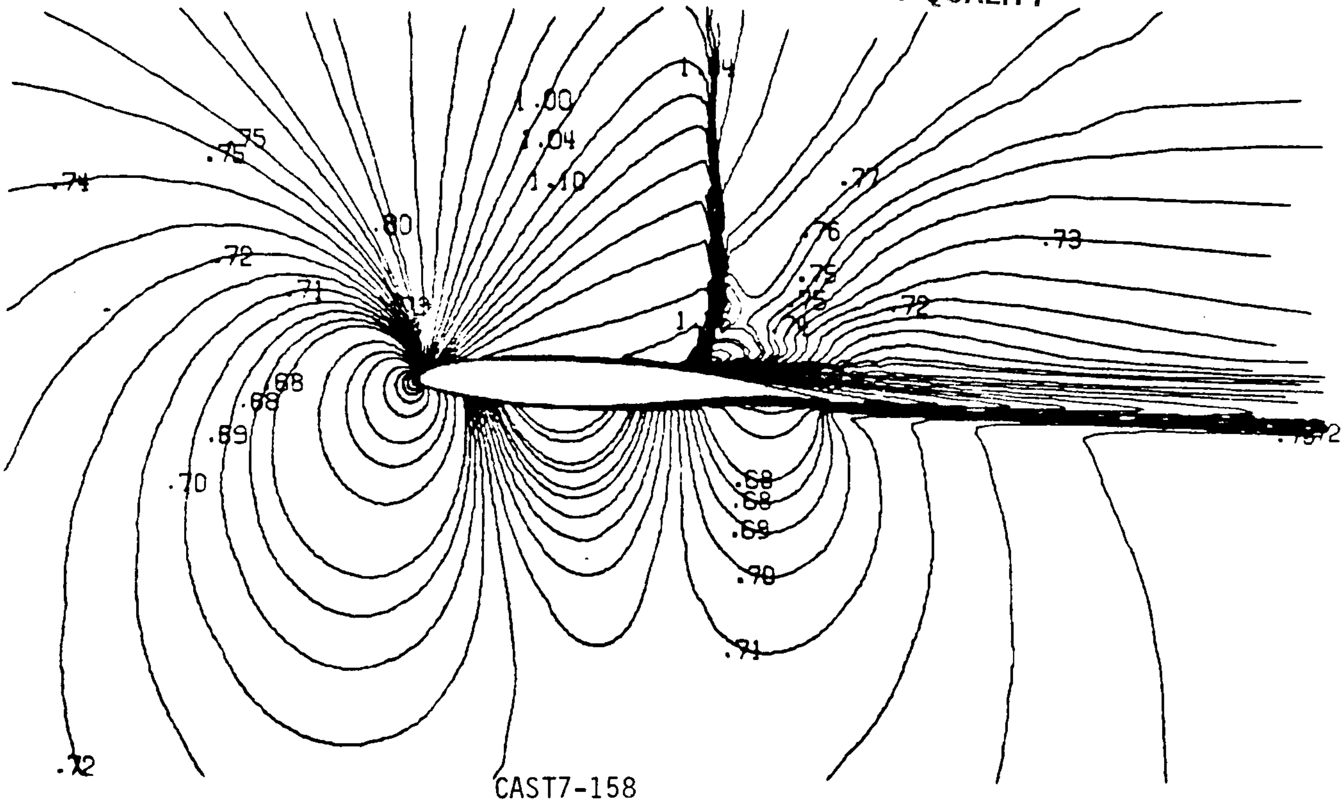

CAST7-158

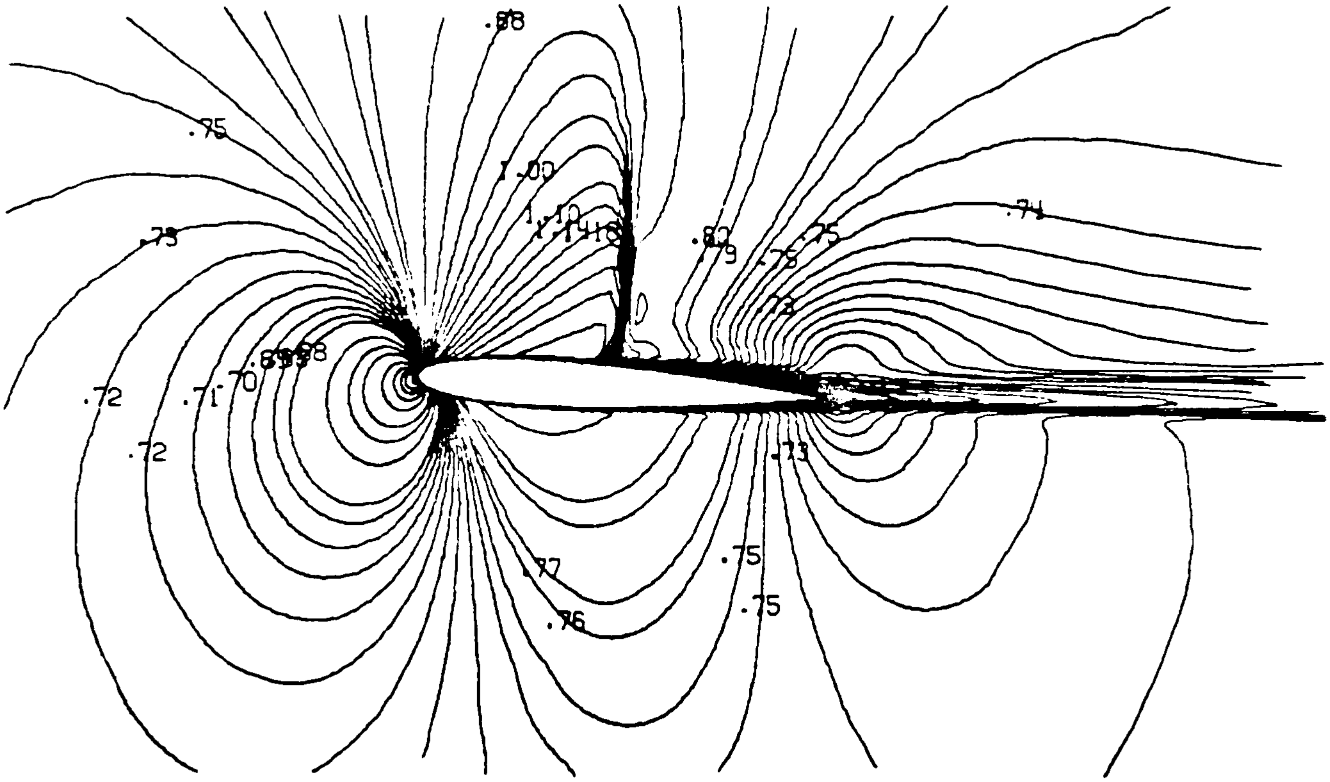

NACA-0012

Fig.10(b) - Mach contours for CAST7-158 and NACA-0012 at. y/R=0.90

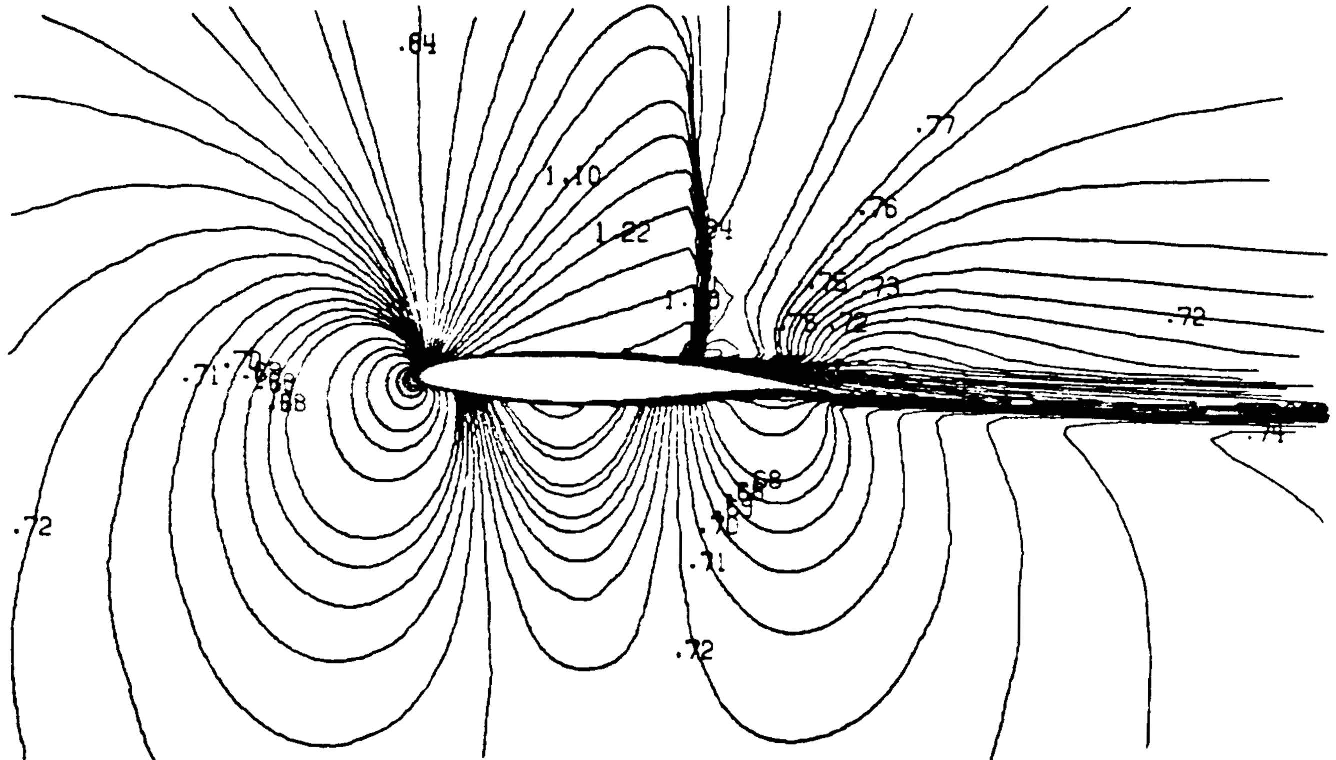

CAST7-158

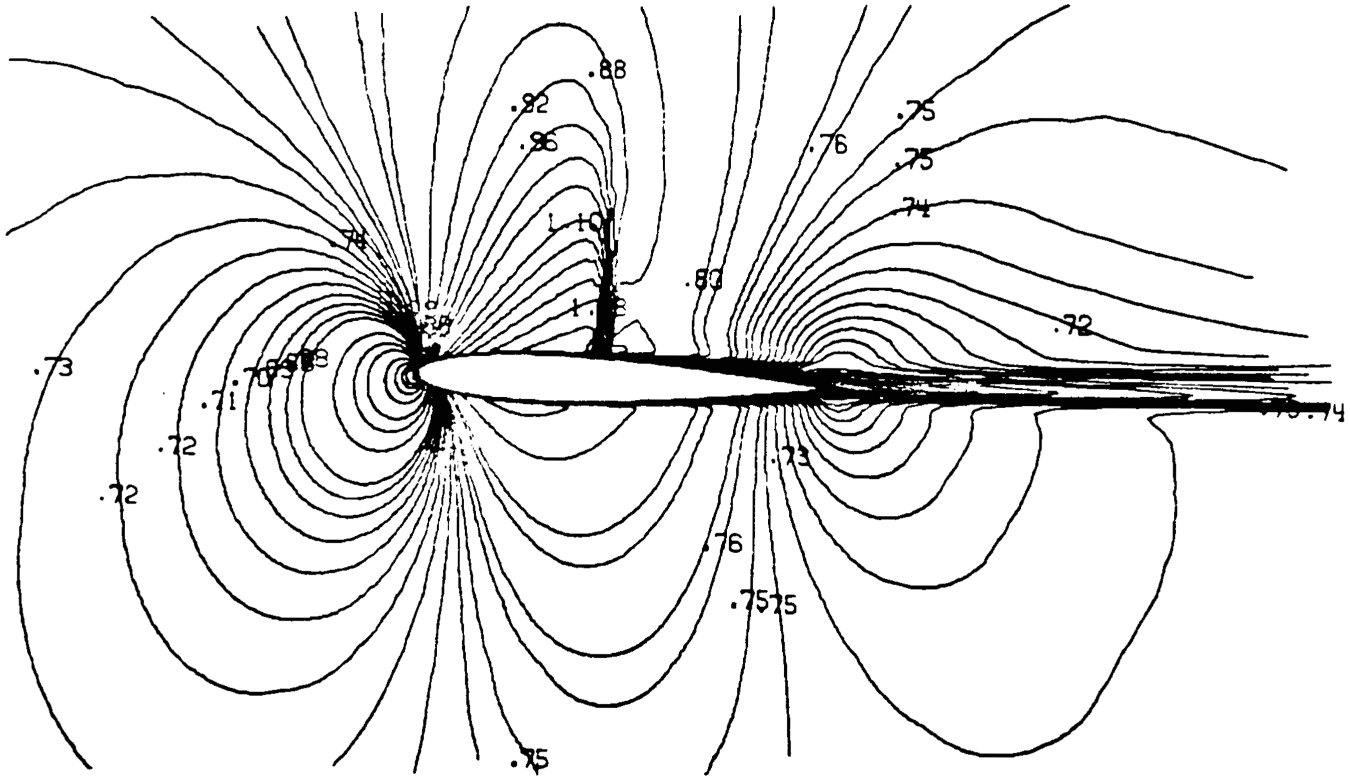

NACA-0012

Fig.10(c) - Mach contours for CAST7-158 and NACA-0012 at y/R=0.80

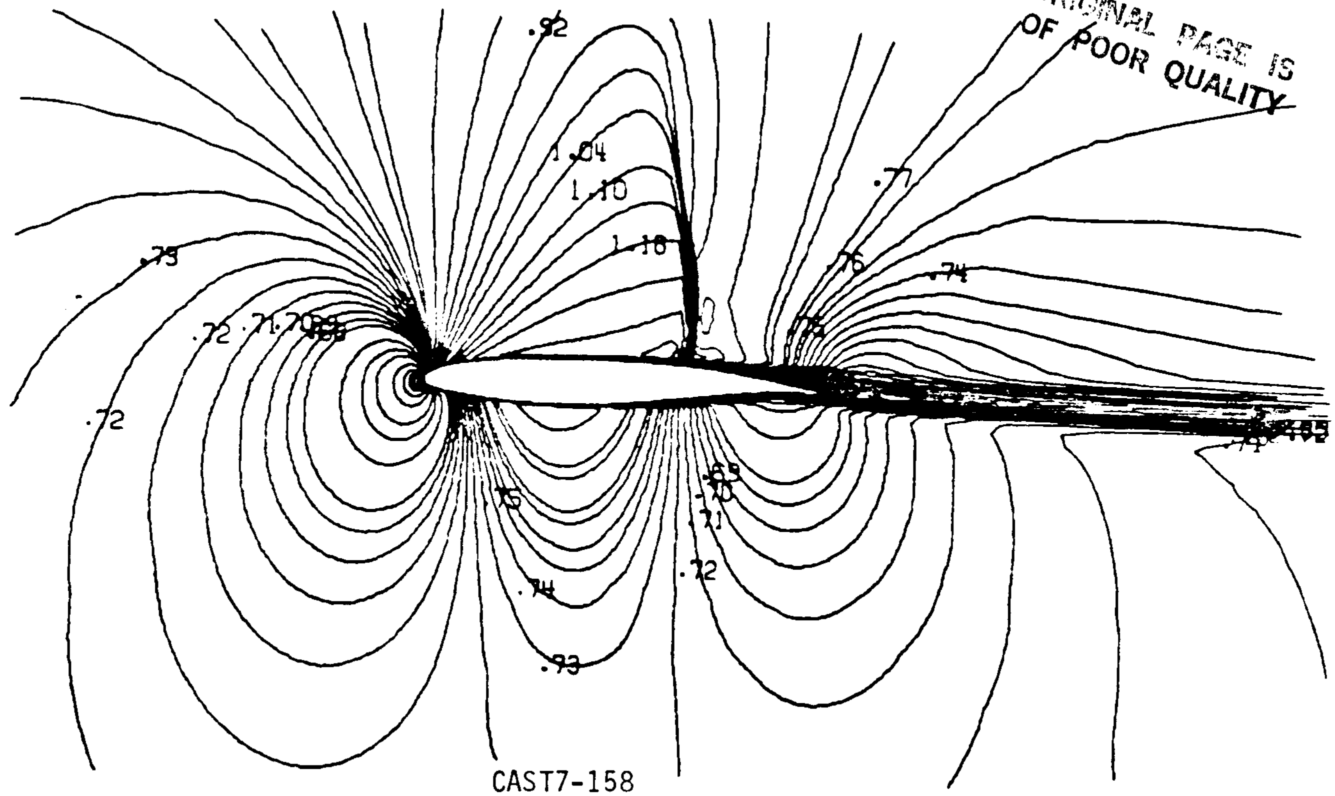

CAST7-158

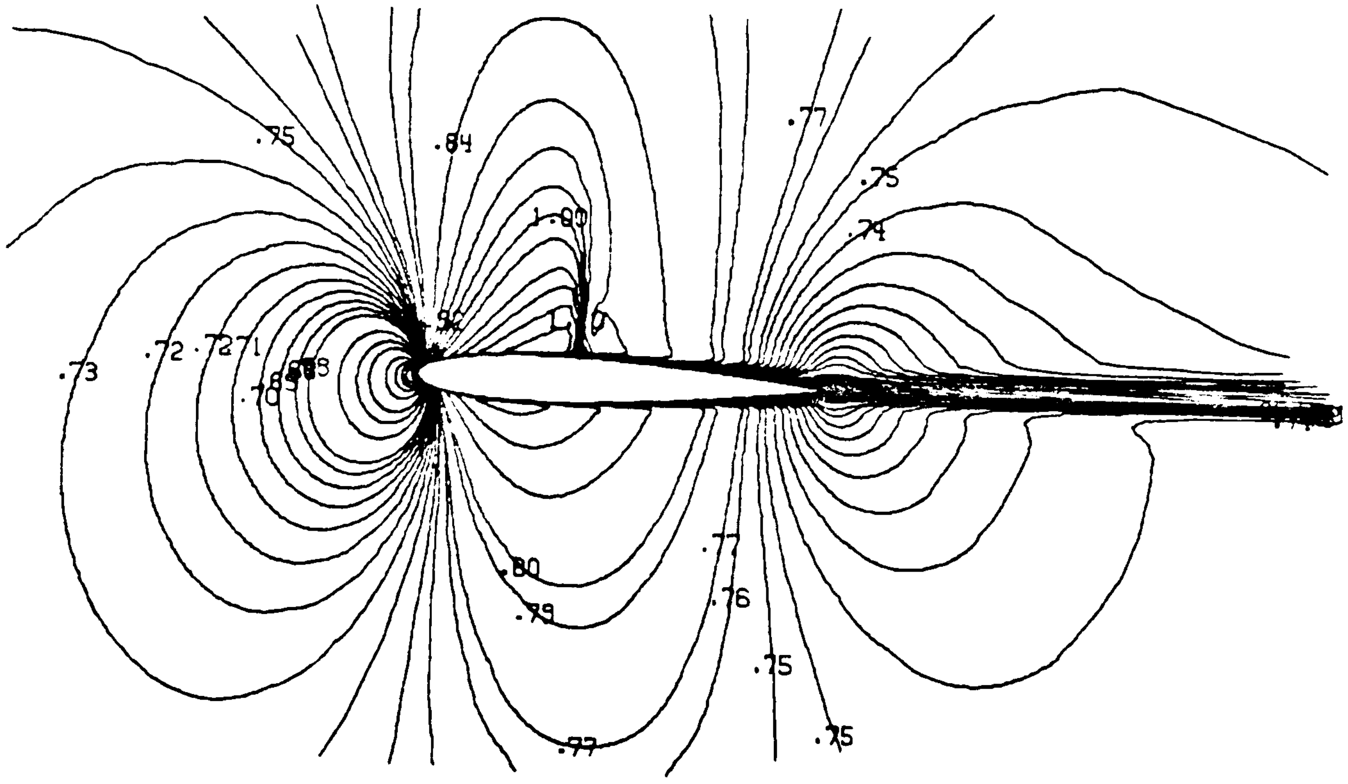

NACA-0012

Fig.10(d) - Mach contours for CAST7-158 and NACA-0012 at y/R=0.70

NASA
National Aeronautics and
Space Administration

Report Documentation Page

1. Report No.
NASA CR-4212

2. Government Accession No.

3. Recipient's Catalog No.

4. Title and Subtitle
Numerical Simulation and Comparison of Symmetrical/Supercritical Airfoils for the Near Tip Region of a Helicopter in Forward Flight

5. Report Date
January 1989

6. Performing Organization Code

7. Author(s)
F. F. Badavi

8. Performing Organization Report No.

10. Work Unit No.
505-63-51-07

9. Performing Organization Name and Address
Planning Research Corporation
Aerospace Technologies Division
303 Butler Farm Road
Hampton, VA 23666

11. Contract or Grant No.
NAS1-18000

12. Sponsoring Agency Name and Address
National Aeronautics and Space Administration
Langley Research Center
Hampton, VA 23665-5225

13. Type of Report and Period Covered
Contractor Report

14. Sponsoring Agency Code

15. Supplementary Notes
Langley Technical Monitor: Robert A. Golub

16. Abstract

Aerodynamic loads on a single-bladed helicopter rotor in forward flight at transonic tip conditions are calculated. The unsteady, three-dimensional, time accurate, compressible Reynolds-averaged thin layer Navier-Stokes equations are solved in an inertial coordinate system on a body-conformed, curvilinear grid of C-H topology. Detailed boundary layer and global numerical comparisons of NACA-0012 symmetrical and CAST7-158 supercritical airfoils are made under identical forward flight conditions. The rotor wake effects are modeled by applying a correction to the geometric angle of attack of the blade. This correction is obtained by computing the local induced downwash velocity with a free wake analysis program. The calculations are performed on the Numerical Aerodynamic Simulation Cray 2 and on the VPS32 (a derivative of a Cyber 205 at Langley Research Center) for a model helicopter rotor in forward flight.

17. Key Words (Suggested by Author(s))
Navier Stokes equations
Boundary layer
Displacement thickness
Momentum thickness
Free-wake analysis
Viscous flux
Prandtl number
Reynolds number

18. Distribution Statement
Unclassified - Unlimited

Subject Category 71

19. Security Classif. (of this report)
Unclassified

20. Security Classif. (of this page)
Unclassified

21. No. of pages
56

22. Price
A04

NASA FORM 1626 OCT 86

NASA-Langley, 1989

For sale by the National Technical Information Service, Springfield, Virginia 22161-2171